Hindawi Publishing Corporation
International Journal of Antennas and Propagation
Volume 2015, Article ID 264812, 22 pages
http://dx.doi.org/10.1155/2015/264812

Review Article

A Tutorial on Optical Feeding of Millimeter-Wave Phased Array Antennas for Communication Applications

Ivan Aldaya,[1] Gabriel Campuzano,[1] Gerardo Castañón,[1] and Alejandro Aragón-Zavala[2]

[1] *Department of Electrical and Computer Engineering, Tecnológico de Monterrey, Avenida Eugenio Garza Sada 2501, 64849 Monterrey, NL, Mexico*
[2] *Department of Electronics and Mechatronics, Tecnológico de Monterrey, Campus Querétaro, Epigmenio González 500, 76130 Querétaro, QRO, Mexico*

Correspondence should be addressed to Ivan Aldaya; ivan.a.aldaya@ieee.org

Received 14 January 2015; Revised 9 April 2015; Accepted 16 April 2015

Academic Editor: Felipe Cátedra

Given the interference avoidance capacity, high gain, and dynamical reconfigurability, phased array antennas (PAAs) have emerged as a key enabling technology for future broadband mobile applications. This is especially important at millimeter-wave (mm-wave) frequencies, where the high power consumption and significant path loss impose serious range constraints. However, at mm-wave frequencies the phase and amplitude control of the feeding currents of the PAA elements is not a trivial issue because electrical beamforming requires bulky devices and exhibits relatively narrow bandwidth. In order to overcome these limitations, different optical beamforming architectures have been presented. In this paper we review the basic principles of phased arrays and identify the main challenges, that is, integration of high-speed photodetectors with antenna elements and the efficient optical control of both amplitude and phase of the feeding current. After presenting the most important solutions found in the literature, we analyze the impact of the different noise sources on the PAA performance, giving some guidelines for the design of optically fed PAAs.

1. Introduction

Frequency saturation is the *sword of Damocles* hanging over high-capacity wireless systems [1, 2]. With an outstanding increase of bandwidth demand, the provisioning of future wireless broadband multimedia applications is uncertain. In this context, the use of millimeter-wave (mm-wave) frequencies has been long recognized as a solution to this spectrum scarcity issue [3]. Different unlicensed mm-wave bands have been proposed for wireless local area networks (WLANs), for example, WiGig that operates at 60 GHz [4], as well as for wireless personal area networks (WPANs) such as IEEE 802.15c [5] and ECMA387 [6], and multi-Gbps wireless backup [7, 8]. In addition, it is widely accepted that upcoming 5G mobile systems will operate at frequencies far above the UHF band [9, 10]. It goes without saying that migration to higher frequencies opens a new world of opportunities. However, this awesome capacity increase is achieved at the expense of more complex and power hungry electronics and more significant wireless path loss [11]. In this sense, the limited radiation power, alongside higher path losses [12], makes necessary the use of highly directional antennas. Although, in back-haul mm-wave links, antennas can be mechanically oriented, in mobile systems the transmitter must dynamically control the radiation pattern in order to point to the desired receiver. Phased array antennas (PAAs) have the capacity of varying their radiation pattern, a feature known as beamforming, which makes them a key enabling technology for either mm-wave access networks [13] or 5G mobile systems [14]. In addition, for handling path loss while keeping low radiation power, dynamically controlled PAAs provide a higher degree of security [15], improve robustness to multipath [16], and reduce cochannel interference [17], which further enhances the aggregated capacity.

At frequencies below 5 GHz, great advances have been made in compact and low consumption integrated PAAs, making them an everyday reality, that is, in 3G and 4G systems. However, at higher frequencies, the fabrication of broadband low-loss phase delays, required to perform beamforming, poses a serious challenge. First implementations relied on ferrite nucleus that resulted in bulky and heavy arrays [18]. As higher degree of integration was required, array weight and size decreased progressively [19]. Afterwards, microelectromechanical systems (MEMSs) emerged, enabling the implementation of true time delay (TDD) lines, which presented significantly broader bandwidth than ferrite-based phase shifters [20]. In parallel, since the early days of microwave photonics, different optical techniques for controlling the phase of an RF signal were proposed [21, 22]. Optical techniques have the advantages of being able to deal with higher RF frequencies, as well as to present a significantly broader bandwidth and lower losses compared to their electrical counterpart [23], making optical control an attractive approach for mm-wave smart antennas. However, optical feeding still presents two significant challenges: on the one hand, the integration of a fast photodiode (PD) with an antenna requires a thorough design that should pay special attention to power budget analysis. On the other hand, phase and amplitude control of the antenna elements must be done in an efficient way.

Several previous books and tutorials have analyzed PAAs [24] or microwave photonics [21, 22] systems, including some aspects of optical feeding of phased arrays. Reference [25] is devoted completely to the application of photonics in modern radar applications. It includes an extensive review of photonic techniques as well as a detailed background, but it does not consider the particularities of mm-wave systems. The present paper constitutes, to the best of our knowledge, the first work fully devoted to covering the particular problems and challenges of the optical feeding of PAAs operating at mm-wave frequencies. Furthermore, the literature review allowed us to classify the different beamforming architectures, which were compared in terms of their performance. We had two audiences in mind when we wrote this tutorial; it is oriented to antenna engineers that want to get some knowledge on the work done in the optical domain, as well as to optical engineers that require knowing the characteristics of the signals that must be generated. Therefore, this work pretends to be to some extent self-contained, which requires some basic concepts that are included in the paper.

The paper is organized as follows. Section 2 introduces the fundamental concepts required for the rest of the paper, as well as the nomenclature that we will use. Section 3 is dedicated to the integration of fast PDs with antenna elements, whereas Section 4 presents the different optical architectures, as well as particular techniques to control the amplitude and phases of the elements. These architectures are compared in terms of the PAA performance in Section 5. In Section 6, some research opportunities are listed and, finally, Section 7 concludes the paper.

2. Fundamental Concepts

In this section we describe in more detail the PAA and its different types, as well as the expression for its radiation pattern. Later on, beam steering, beam shaping, and beamforming concepts are explained. On the other hand, the optical generation of RF signals is presented, paying special attention to the phase noise of the generated RF signal.

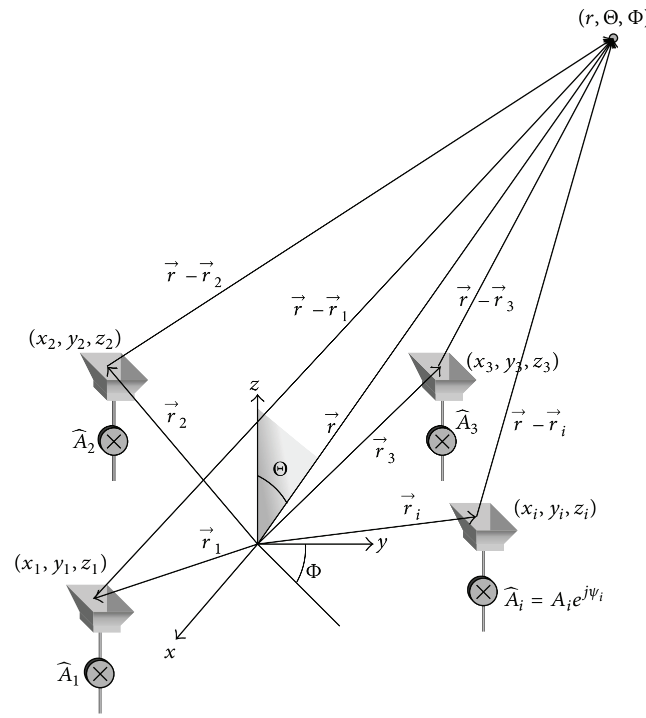

Figure 1: Sketch of a PAA for the calculation of its radiation pattern. Θ: azimuthal angle; Φ: elevation angle; $\vec{r} = (r, \Theta, \Phi)$: position of the point of interest in spherical coordinates; vec$r_i = (x_i, y_i, z_i)$: position of the ith antenna element; $\widehat{A}_i$ complex amplitude of the feeding currents, which can be expressed in terms of the real-valued amplitude, A_i, and phase, ψ_i.

2.1. Phased Array Antennas. The scheme of a PAA is a collection of coherently radiating elements that can be independently fed [26]. The elements, which are usually identical, are therefore fed with signals at the same frequency but with possibly different phases and amplitudes. PAAs can be classified according to different features: if each element has a dedicated oscillator, then the PAA is said to be *active* [27], in contrast to *passive* phased arrays, where all the feeding currents derive from the same oscillator. Depending on the geometrical configuration, a PAA can be *linear*, if the antenna elements are arranged in a line, *planar*, if they are in a plane, or *conformal*, when the elements are placed on a 3D surface. *Uniform* PAAs are those where the element positions conform to a regular grid, whereas *nonuniform* PAAs are arrays with an irregular grid [17]. When the amplitudes relation and relative phases of the feeding currents do not vary on time, the PAA is *static*, whereas when phases and amplitudes of the elements are varied, it is denominated *dynamic* PAA. By a proper design, PAAs present high gain and dynamic flexibility that justify them as a key element in modern communication systems.

A general PAA is sketched in Figure 1, where the position of the ith antenna element is denoted by $\vec{r}_i = (x_i, y_i, z_i)$ and the complex amplitude of the feeding current by $\widehat{A}_i = A_i e^{j\psi_i}$. The radiation pattern of the N-element PAA can be found applying the superposition principle at an arbitrary position

$\vec{r} = (r, \Theta, \Phi)$. The total electrical field strength at $\vec{r}$ can be expressed as

$$E(\vec{r}) = \sum_{i=1}^{N} E_i(\vec{r}) = \sum_{i=1}^{N} \sqrt{\frac{2\eta_0 G(\Theta,\Phi)}{4\pi}} A_i e^{j\psi_i} \frac{e^{j2\pi|\vec{r}-\vec{r}_i| f_{\mathrm{RF}}/c}}{|\vec{r}-\vec{r}_i|}, \tag{1}$$

where $E_i(\vec{r})$ is the contribution of the ith element, η_0 is the intrinsic impedance of the vacuum, $G(\Theta, \Phi)$ is the gain of each element as a function of the elevation angle Θ and azimuthal angle Φ, f_{RF} denotes the operation frequency, and c denotes the speed of light in the vacuum. The previous expression can be rearranged grouping the terms related to the amplitude and phase:

$$E(\vec{r}) = \underbrace{\sum_{i=1}^{N} \sqrt{\frac{2\eta_0 G(\Theta,\Phi)}{4\pi |\vec{r}-\vec{r}_i|^2}} A_i}_{\text{Amplitude term}} \underbrace{e^{j(\psi_i + 2\pi|\vec{r}-\vec{r}_i| f_{\mathrm{RF}}/c)}}_{\text{Phase term}}. \tag{2}$$

In the far-field region, also known as *Fraunhofer* region, $|\vec{r}| \gg |\vec{r}_i|$ and, therefore, $|\vec{r}-\vec{r}_i| \approx |\vec{r}| = r$; that is, the fields radiated by the different elements are attenuated in the same way. This is not the case of the phase, where the phase differences lead to an interference pattern. The phase of each contribution is composed of the phase of the feeding amplitude, ψ_i, and a space-dependent term, $2\pi|\vec{r}-\vec{r}_i| f_{\mathrm{RF}}/c$, that can be written in terms of the element coordinates according to

$$\psi_i'(\vec{r}) = \frac{2\pi f_{\mathrm{RF}}}{c} (\sin\Theta \cdot (x_i \cos\Phi + y_i \sin\Phi) + z_i \cos\Theta). \tag{3}$$

If the PAA is correctly designed to avoid mismatching among its elements [28], after far-field approximation, and taking the common factor out of the summation, the electric field strength acquires the following form:

$$E(\vec{r}) = \sqrt{\frac{2\eta_0 G(\Theta,\Phi)}{4\pi r^2}} \cdot \sum_{i=1}^{N} A_i e^{j(\psi_i + \psi_i')}. \tag{4}$$

The first factor in (4) depends only on the antenna element and the spatial coordinates through the element radiation pattern. On the contrary, the second term does not depend on the characteristics of the antenna element but on their arrangement and feeding, that is, A_i and ψ_i. It is denoted as *array factor* (AF) and represents the spatial interference among the different elements of the array:

$$\mathrm{AF}(\Theta,\Phi) = \sum_{i=1}^{N} A_i e^{j(\psi_i + \psi_i')}. \tag{5}$$

In PAAs, the position and shape of the elements are typically fixed and, therefore, the radiation pattern is controlled through the feeding of the elements, varying either their

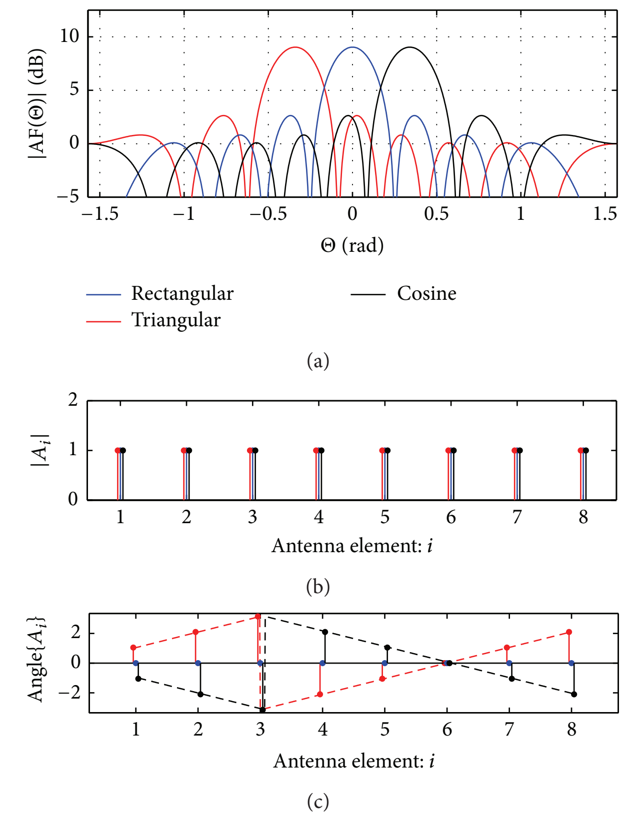

Figure 2: Beam steering through phase control of an 8-element linear array. (a) Resulting AF for $\Phi = 0$, (b) amplitudes of the weights, and (c) the phase of the elements.

amplitudes, phases, or both of them. The radiation pattern of the PAA can be expressed in terms of the AF as

$$G_{\mathrm{PAA}}(\Theta,\Phi) = G(\Theta,\Phi) \frac{|\mathrm{AF}(\Theta,\Phi)|^2}{\sum_{i=1}^{N} |A_i|^2}. \tag{6}$$

Usually, in PAA systems, the antenna elements are not very directional since, otherwise, the PAA could be only directed within a narrow range [29]. Under this assumption, the radiation pattern of the elements can be considered isotropic and the gain of the PAA is then given mainly by the AF term. Therefore, it can be approximated by

$$G_{\mathrm{PAA}}(\Theta,\Phi) \approx \frac{|\mathrm{AF}(\Theta,\Phi)|^2}{\sum_{i=1}^{N} |A_i|^2}. \tag{7}$$

By controlling the amplitude and phase of each element feeding current, both beam steering (controlling the direction of maximum radiation) and beam shaping, as well as the more general beamforming, can be implemented. Both beam steering, Figure 2, and beam shaping, Figure 3, using a 1×8 linear PAA are shown. Beam steering is usually accomplished by applying the same amplitudes to the different antenna elements and setting linearly increasing/decreasing phases, as can be seen in Figures 2(b) and 2(c). In linear PAAs, these phases can be achieved applying a differential time delay, τ,

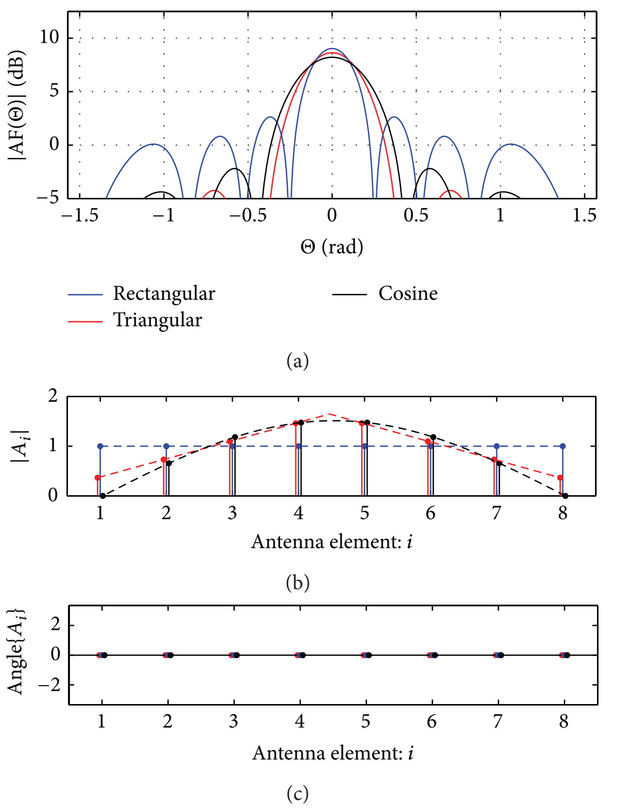

Figure 3: Beam shaping through amplitude control of an 8-element linear array. (a) Resulting AF for $\Phi = 0$, (b) amplitudes of the weights, and (c) the phase of the elements.

which is related to the desired angle of maximum radiation [30]:

$$\Theta_{\text{MAX}} = \sin\left(2\tau f_{\text{RF}}\right). \quad (8)$$

On the other hand, beam shaping is typically performed by applying different current amplitudes to antenna elements. Figures 3(b) and 3(c) show the amplitudes and phases of the feeding currents of the PAA elements. Uniform amplitudes result in the highest gain, that is, the narrowest main lobe. When the amplitudes of the elements are modulated, the lobe is wider and the gain reduced. However, it is important to note that the amplitude of the sidelobes is significantly reduced, which can be important for some applications. In addition, the nulls of the radiation pattern can be set at desired position, avoiding interference.

From an implementation point of view, the phase and amplitude of the currents can be calculated employing a digital signal processor or can be selected from a preconfigured table [17]. The former, denominated *adaptive antennas*, presents better performance since it can adapt more precisely to the channel, being able to carry out interference avoidance, but may require complex algorithms. The latter, named *beam switching*, is less complex, but the degree of precision to point the main lobe is not so good.

2.2. Photonic Generation of mm-Wave Signals. In recent years, a plethora of photonic mm-wave generation techniques have been proposed [31, 32]. A literature review reveals the significant effort of different research groups to reduce the size and complexity while increasing the power efficiency of photonic mm-wave generators. First generation techniques based on modulating a free-running laser [33] soon became obsolete due to their narrow bandwidth. They were overcome by optical sideband injection locking [34, 35] and modulation of lasers subject to strong optical injection [36]. However, although these techniques present exceptional performance in terms of spectral purity, they are difficult to configure and require relatively precise temperature control [21]. With the advances in broadband modulators, techniques based on external modulation gained popularity, especially those employing frequency multiplication, which relaxed the bandwidth requirements of both the modulator and the associated electronics [37]. Furthermore, external modulation showed its full potential with the advection of photonic chips that integrated the laser source together with an electroabsorption modulator [38]. Simultaneously, mm-wave generators based on alternative approaches have been investigated, for instance, in [39] where a passive mode-locked laser is used to avoid the high-frequence electrical oscillator. In this case, all the modes of the laser are modulated with the same information but different modes can be used to simultaneously generate multiple RF signals [40]. If a high number of antenna elements are to be fed, the number of high power modes of a semiconductor mode-locked laser would be insufficient. In such cases, optical comb generators based on highly nonlinear devices may be employed [41]. This technique requires an optical amplifier and is difficult to integrate but it is capable of generating more than 1000 highly correlated tones with 50 GHz frequency separation. In conclusion, the broad variety of photonic mm-wave generation techniques can be exploited to meet the required specifications, either low cost or high number of channels.

Figure 4 shows a simplified photonic mm-wave generation and distribution system, alongside the spectra at different stages of the system. The mm-wave signal is generated by beating at PD spectral components separated by the desired RF frequency. Even if some previous papers propose the generation of mm-wave signals using several modulated fields [39, 42], optical single sideband (OSSB) modulation, composed of two optical fields, one unmodulated and the other modulated with the information signal, is preferable since it is more robust to fiber dispersion [43]. An OSSB signal can be expressed mathematically as

$$\begin{aligned} E(t) = {} & E_{01}(t) \cdot \exp\left\{j\left[2\pi f_1 t + \phi_1(t)\right]\right\} + m(t) \\ & \cdot E_{02}(t) \cdot \exp\left\{j\left[2\pi f_2 t + \phi_2(t)\right]\right\}, \end{aligned} \quad (9)$$

where f_1 and f_2 are the optical frequency of the unmodulated and modulated fields, respectively, being related through $|f_2 - f_1| = f_{\text{RF}}$. $E_{01}(t)$ and $E_{02}(t)$ are the real-valued amplitudes accounting for the intensity fluctuation, whereas $m(t)$ is a complex modulating signal that allows modeling both amplitude and in-phase/quadrature modulations. $\phi_1(t)$ and $\phi_2(t)$ are the phase noise of both fields, which are typically modeled as Wiener processes [44].

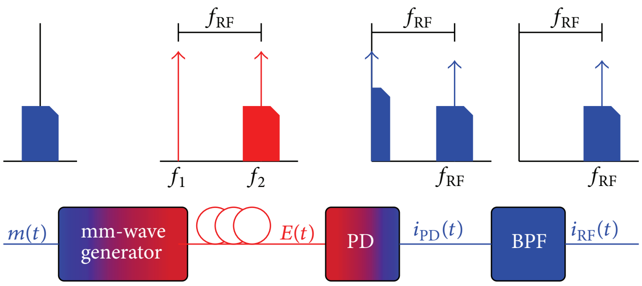

FIGURE 4: Photonic mm-wave generation and distribution system and spectra at different stages of the system.

The OSSB signal is detected by a photodetector (PD) with a bandwidth exceeding f_{RF}. Given the quadratic response of the PD to the incident optical field, the photogenerated current, $i_{\mathrm{PD}}(t)$, is proportional to the square of the field modulus:

$$i_{\mathrm{PD}}(t) = R|E(t)|^2 + n(t) = R[E(t)\cdot E(t)^*] + n(t), \quad (10)$$

where the responsivity, R, and the noise of the PD, $n(t)$ that is considered as an additive white Gaussian noise (AWGN) accounting for both the thermal and shot noise. The photogenerated current consists of low-frequency components that are filtered out by a band-pass filter (BPF) and a signal around f_{RF}, which acquires the following expression:

$$\begin{aligned} i_{\mathrm{RF}}(t) &= R\cdot E_{01}(t)E_{02}(t) \\ &\cdot (\mathrm{Re}\{m(t)\}\cos[2\pi f_{\mathrm{RF}}t + \Delta\phi(t)] \\ &\cdot \mathrm{Im}\{m(t)\}\sin[2\pi f_{\mathrm{RF}}t + \Delta\phi(t)]) + n'(t), \end{aligned} \quad (11)$$

or in a more compact form

$$\begin{aligned} i_{\mathrm{RF}}(t) &= R\cdot E_{01}(t)E_{02}(t)\cdot|m(t)| \\ &\cdot \cos[2\pi f_{\mathrm{RF}}t + \phi_m(t) + \Delta\phi(t)] + n'(t). \end{aligned} \quad (12)$$

In (12), $|m(t)|$ and $\phi_m(t)$ represent the amplitude and phase of the modulating signal $m(t)$, respectively. Therefore, the generated signal is corrupted by amplitude fluctuations, which is mainly caused by the lasers' relative intensity noise (RIN), the filtered AWGN, $n'(t)$, and the phase noise $\Delta\phi(t)$ given by $\phi_2(t) - \phi_1(t)$. Hence, $\Delta\phi(t)$ depends on both individual statistical properties of $\phi_1(t)$ and $\phi_2(t)$ and their correlation properties. The spectral properties of the photogenerated current have been studied in detail in [44, 45], from which two particular cases can be distinguished: when $\phi_1(t)$ and $\phi_2(t)$ are completely decorrelated, the generated signal presents a significant phase noise. If distributed feedback (DFB) lasers with linewidth in the order of MHz are used, the phase noise will be the limiting impairment degrading the signal quality. When the fields have correlated phase noises, they compensate each other and RF carriers with high spectral purity are generated. Highly correlated tones can be achieved by using external modulation [46], by using fields generated within the same laser cavity [40], or by means of optical injection locking of two lasers to a common master laser [47]. In particular, depending on the PAA feeding architecture, the system may be very sensitive to the phase noise of the RF signal, since, as already discussed, the shape of the radiation pattern varies with the phase difference among antenna elements.

3. Antenna Integration with High-Speed PDs

Antenna integration is a key factor in building compact and low-cost PAAs. We first present the different antenna integration techniques and then the state-of-the-art high output power and broad-bandwidth PDs. Afterwards some issues related to the PD-antenna integration are discussed.

3.1. Integrated Phased Arrays. The significant research effort has made integrated antennas a reality in everyday life. There is no need to be very old to remember mobile terminals with extensible antennas. It is not only a matter of aesthetics but mainly an issue of cost and reliability. Design maturity allows antennas to operate at difference bands with high efficiency at frequency below 10 GHz. We can distinguish two main types of integrated antennas: (i) coplanar antennas, where the antenna and the ground plane are at the same level [48], Figure 5(a), and (ii) multilayer antennas, where the feeding networks (including the phase shifters and amplitude controllers) are at different planes [49], which are shown in Figure 5(b). Typically, coplanar antennas are cheaper and easier to manufacture since a single metal layer is required; however, as operation frequency increases, the isolator-induced losses result in a poor efficiency. At mm-wave frequencies, where power efficiency is critical, the multilayer approach is preferable. In this sense, the feeding network is built on a highly conductive semiconductor substrate, while antenna elements can be built using a lower conductivity semiconductor layer [50]. Between the feeding network layer and the antenna layer a low density isolator (often denominated foam) is placed in order to further reduce the losses. The connection between both semiconductor layers is typically accomplished using wire-like structures; however, at high frequencies, coupling structures have been shown to improve the array performance [51].

3.2. High-Speed PDs. Given the band structure of the silicon, with a band gap of 1.11 μm, it is transparent in both 2nd and 3rd optical communication windows (i.e., at 1300 and 1550 nm). However, in recent years impressive advances in Si-based PDs have been made: in [52] a SiGe PD with a 6.28 GHz bandwidth is presented and, more recently, a Selenium doped PD exhibiting 20 GHz bandwidth was reported [53]. Nevertheless, despite such breakthroughs, bandwidth in the order of mm-wave has only been achieved using III–V elements: InP, GaAs, and other ternary or quaternary combinations [54].

Typically, PDs are composed of three semiconductor layers: a P-doped layer, an intrinsic layer, and an N-doped layer, as shown in Figure 6(a). When the PD is illuminated by a light beam, some of the incident photons interact with the semiconductor (mainly within the intrinsic layer) and are

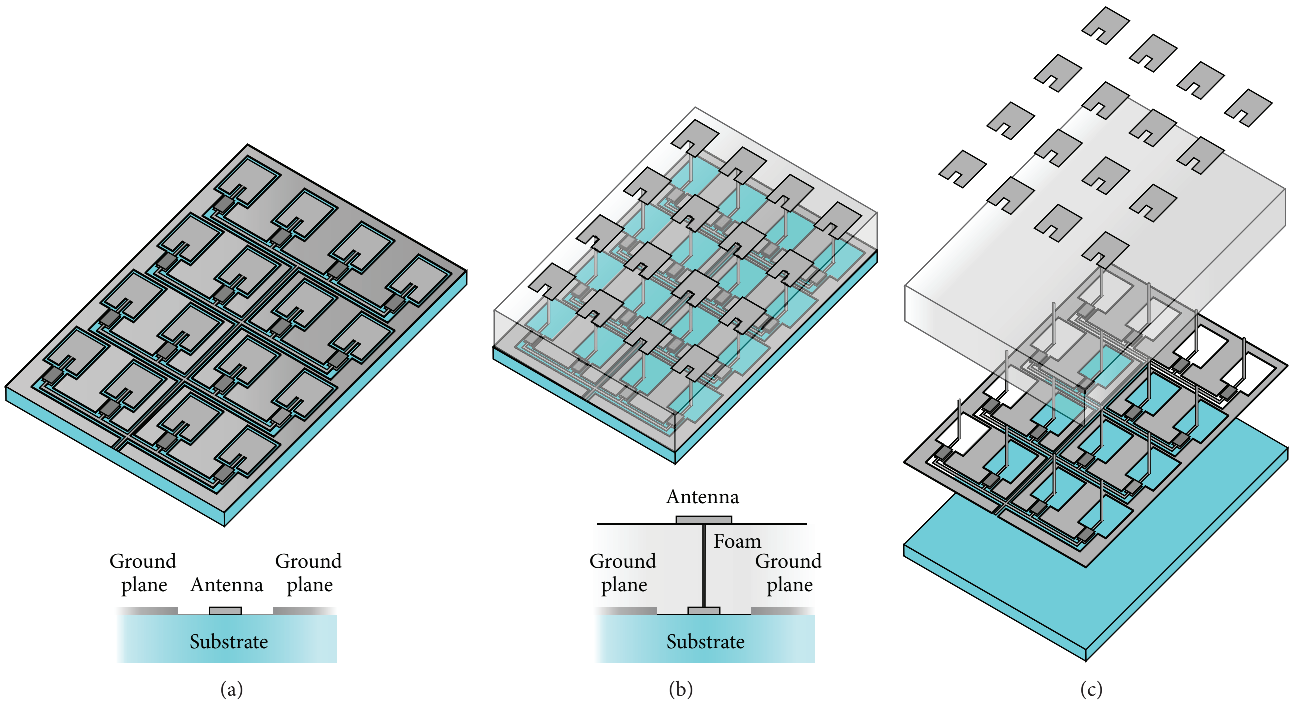

Figure 5: Antenna integration techniques: (a) coplanar antenna and (b) multilayer antenna. (c) Deconstruction of a multilayer antenna.

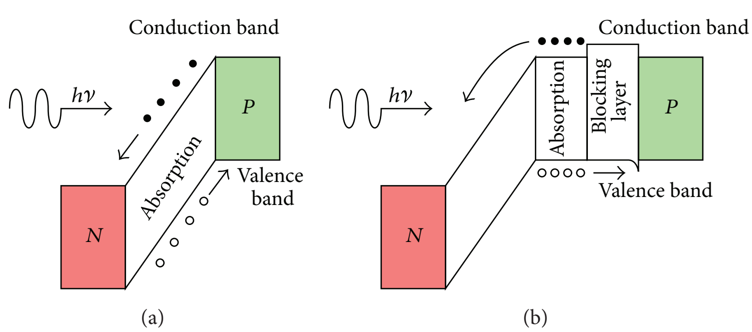

Figure 6: Different PD structures: (a) PIN-PD and (b) UTC-PD.

annihilated generating a hole-electron pair, through the so-called photoelectric phenomenon. The holes and electrons are drifted by an applied electric field, which generates a current proportional to the incident optical power [55]. The fundamental bandwidth of the PD is limited by the diffusion time, which is the time required by the generated holes and electrons to reach the electrodes. This time can be reduced by shortening the intrinsic layer of the PD, but this results in a significant efficiency reduction, and consequently the dynamic range also decreases. Alternatively, diffusion time can be reduced if only high-mobility carriers are used. Uni-travelling carrier (UTC) PD, which is shown in Figure 6(b), blocks the diffusion of holes and uses only electrons as active carriers for photogeneration [56, 57]. UTC-PD has proved exceptional performance in terms of output power and bandwidth: in [58], 20 mW is achieved with a 3-dB bandwidth of 100 GHz. Recently, a more refined scheme is reported with enhanced power and bandwidth, 25 μW and 0.9 THz [59].

3.3. Issues with the PD-Antenna Integration. Antenna integration with high-speed PDs poses two main issues: on the one hand, the impedance matching must be ensured. This can be achieved by well-known microstrip impedance matching networks [60]. In [61] the integration of a UTC-PD with a CPA antenna is reported, whereas in [56, 57] integration with multilayer antenna is presented; in [56] a log-periodic antenna is used, whereas in [57] a path antenna is used. On the other hand, integration of antennas with PDs makes the inclusion of power amplifier between the PD and the antenna extremely difficult. Consequently, the radiated power is limited by the PD power performance. However, the use of PAA helps in overcoming this power limitation.

As stated, the power radiated by each element is limited by the output power of the PD and is given by

$$P_{\text{element}} = e_0 \cdot P_{\text{output}}, \tag{13}$$

where e_0 is the antenna efficiency accounting for the impedance mismatch, as well as the ohmic loss, and P_{output}

is the power delivered by the PD in linear units. However, the maximum radiated power radiated by an N-element PAA is higher:

$$P_{\text{total}} = N \cdot P_{\text{element}}. \quad (14)$$

And the equivalent isotropic radiated power (EIRP) in linear units results to be

$$\text{EIRP} = P_{\text{total}} \cdot G_{\text{PAA}}\big|_{\max}. \quad (15)$$

Therefore, increasing the number of antenna elements has a twofold effect: first, the total radiated power grows linearly with the number of elements and, second, since the maximum gain of the PAA increases as the number of elements does, the EIRP is further enhanced. A higher number of elements, however, typically results in significant splitting loss in the optical distribution network, which may require optical amplification that is relatively easy to integrate with the PD array.

4. Optical Beamforming

Given the necessity for configurable radiation patterns, beamforming has attracted an increasing attention. Particularly, a lot of effort has been dedicated to the design of broad-bandwidth optical beamforming circuits, which typically rely on true time delays (TTDs) [62]. In systems operating at few GHz, digital implementation of TTDs has emerged as a flexible solution that outperforms analog implementation both in steering speed and flexibility, with similar power consumption [63]. In systems operating at mm-wave frequencies, analog-to-digital and digital-to-analog conversions are prohibitively expensive and power consuming and, consequently, digital TTDs are not feasible and analog TTDs are challenging. Since in the optical domain broadband TTDs are relatively easy to implement, optical beamforming appears as an attractive approach [64]. In this section we review some of the most promising approaches both for amplitude and phase control.

4.1. Optical Architecture for Feeding Antenna Elements. An optical feeding architecture is typically composed of several subsystems: single or multiple photonic mm-wave generators, an optical beamforming network (OBFN), an optical distribution network (ODN), and the antenna unit that includes the phased array alongside the broad-bandwidth PDs. The photonic mm-wave generator is responsible for generating the optical signal that, when detected at the PD, results in the desired mm-wave signal. In the OBFN, the phases and amplitudes of the optical tones are modified in order to control the AF of the PAA, whereas the ODN is used to communicate signals either from the mm-wave generator to the OBFN, in the case of on-site beamforming, or from the OBFN to the antenna unit if centralized control is used. Typically, the ODN accounts for passive elements such as splitters and fiber, as well as amplifiers that enable longer distance or higher radiated power. Photonic feeding architectures can be divided between those with on-site OBFN and those with centralized OBFN. On the other hand, some architectures use the same wavelength to feed the different antenna elements while some other architectures have a dedicated wavelength for each antenna element. The latter can be further classified according to the mm-wave generation type, that is, if the different optical signals are generated using multiple mm-wave generators or a single generator based on a multiwavelength source.

4.1.1. Optical Feeding Architectures Using a Single Wavelength. Figure 7 shows architectures (a) with centralized OBFN and (b) with on-site OBFN. The most striking advantages of these architectures are the lack of demultiplexing/multiplexing devices and a relaxed frequency stability requirement. In comparison, centralized beamforming is preferable since the optical amplifier is shared by the different antenna elements while on-site beamforming requires multiple parallel ODNs, which increases the system cost. However, the splitting loss in the case of on-site OBFN may limit the number of elements to be fed.

4.1.2. Optical Feeding Architectures Using Multiple Wavelengths. The use of multiple wavelengths, typically one per antenna element, offers the possibility to multiplex the different signals into a single fiber. Unfortunately, the advantages derived from multiplexing are achieved at the expense of a huge occupied spectrum, which hinders the feeding of multiple base stations using a single fiber. In Figure 8, different schemes are presented: single mm-wave generator with on-site OBFN, Figure 8(a), and centralized OBFN, Figure 8(b), as well as architectures using multiple mm-wave generators with on-site OBFN, Figure 8(c), and centralized OBFN, Figure 8(d). The higher complexity of multiwavelength mm-wave generators is countervailed by the reduction of the number of required temperature control modules.

4.2. Photonic Control of Feeding Amplitudes. Most of the reported works in the literature focus on optical phase control, obviating amplitude control. This can be attributed to the *a priori* simple implementation, but it still deserves some attention. The amplitude can be controlled in two different ways: by directly controlling the emission power of the mm-wave generator(s) or by means of variable optical attenuators. The power control can operate on one of the two beating tones, or in both of them, depending on the mm-wave generation technique.

4.2.1. Amplitude Control through the Emission Power of the mm-Wave Generators. This approach is cost efficient since it does not require additional optical devices, but it is limited to feeding architectures where each antenna element is fed by an independent mm-wave generator. That is, it is not suitable if a single source is used. Additionally, in many cases, the variation of the bias of the optical sources within the mm-wave generator leads to a frequency deviation because of the coupling between the real and imaginary parts of the refractive index in the semiconductor [65, 66]. If the two beating fields are shifted by a different amount, the resulting

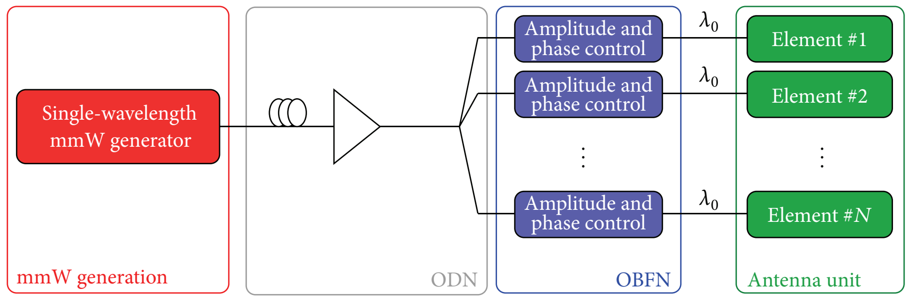

(a)

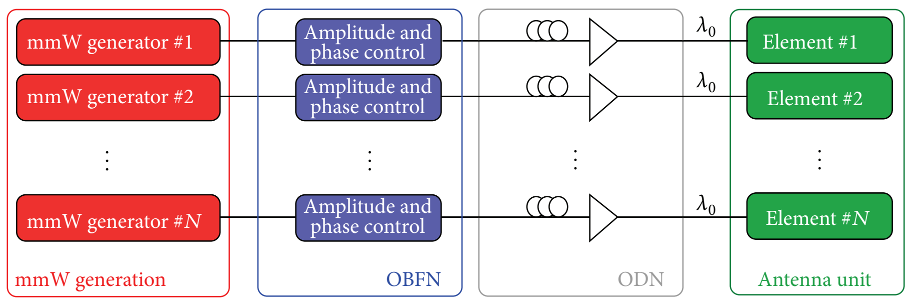

(b)

FIGURE 7: Optical feeding architectures using a single wavelength: (a) on-site beamforming and (b) centralized beamforming. ODN: optical distribution network; OBFN: optical beamforming network.

RF frequency differs from the nominal frequency, degrading the system performance.

4.2.2. Amplitude Control through Variable Optical Attenuator. It is obvious that amplitude control based upon optical attenuators is more expensive than the control based on driving current. In addition, it is *a priori* more complicated to integrate and adds some insertion losses; but it presents some advantages that justify its adoption: it does not affect the frequency of the optical signals and it can be employed even if a multiwavelength mm-wave generator is used. This technique can be implemented using different types of variable optical attenuators, such as $LiNb_3$-based modulators [67] or more integrable semiconductor based modulators [68].

4.3. Photonic Control of Feeding Phases. The photonic control of the phases of PAA elements has attracted more attention than amplitude control because of the bandwidth limit of the electrical phase shifters. Consequently, many different optical techniques can be found in the literature. In some cases, the phase is controlled directly in the optical generation process [69, 70], which results in nonlinear phase control, but, in most cases, an optical true time delay (TTD) is applied after the optical signal is generated. Phase control using TTD is linear in the sense that it does not exploit any nonlinear mechanism that depends on the power of the incident light. Therefore, it is more flexible and simple, being more suitable for real applications. When employing TTDs, the phase control of the antenna element is achieved delaying the optical beating components. Neglecting the phase noise, the electrical field before photo detection can be expressed as

$$\begin{aligned} E(t) &= E_1(t-\Delta T_1) + E_2(t-\Delta T_2) \\ &= E_{01}\exp[j2\pi f_1(t-\Delta T_1)] \\ &\quad + E_{02}\exp[j2\pi f_2(t-\Delta T_2)], \end{aligned} \tag{16}$$

where ΔT_1 and ΔT_2 are the delays applied to each component. The RF photogenerated current then acquires the form of

$$\begin{aligned} i_{RF}(t) &= 2R\cdot E_{01}E_{02} \\ &\quad \cdot\cos[2\pi f_1(t-\Delta T_1) - 2\pi f_2(t-\Delta T_2)]. \end{aligned} \tag{17}$$

We can define two delay times, $\Delta T = (\Delta T_2 + \Delta T_1)/2$ and $\delta T = \Delta T_1 - \Delta T_2$, corresponding to the common-mode delay and the differential delay, respectively. In this way, the common-mode delay accounts for the average delay induced in both fields whereas the differential delay represents the delay difference between components. Rearranging the previous expression in terms of the common-mode and differential delay, we get

$$\begin{aligned} i_{RF}(t) &= 2R\cdot E_{01}E_{02} \\ &\quad \cdot\cos\left[2\pi f_{RF}(t-\Delta T) - 2\pi\frac{f_1+f_2}{2}\delta T\right] \\ &= 2R\cdot E_{01}E_{02}\cdot\cos[2\pi f_{RF}t - \Delta\phi_{CM} - \Delta\phi_{diff}]. \end{aligned} \tag{18}$$

In this expression two phase shifts can be identified, one associated with the common-mode delay, $\Delta\phi_{CM}$, and

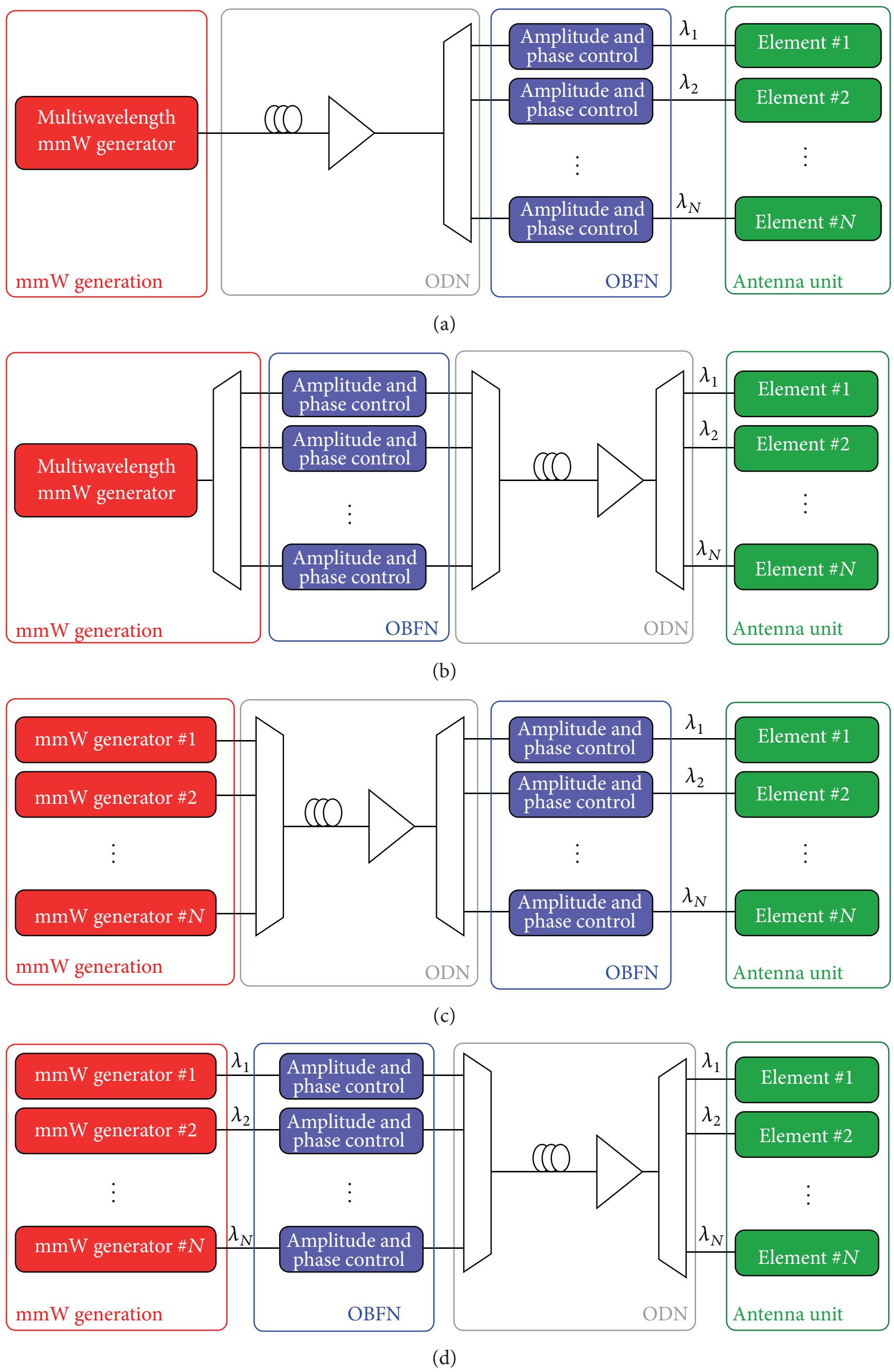

FIGURE 8: Optical feeding architectures using multiple wavelengths: (a) on-site beamforming with a multiwavelength source, (b) centralized beamforming with a multiwavelength source, (c) multiple mm-wave generators with on-site beamforming, and (d) multiple mm-wave generators with centralized beamforming. ODN: optical distribution network; OBFN: optical beamforming network.

the other related to the differential delay, $\Delta\phi_{\text{diff}}$, which can be written as

$$\Delta\phi_{\text{CM}} = 2\pi f_{\text{RF}} \Delta T, \quad (19)$$

$$\Delta\phi_{\text{diff}} = 2\pi \frac{f_1 + f_2}{2} \delta T. \quad (20)$$

There are two important points to note here: first, the phase of the generated RF signals can be controlled either delaying single or both beating components. Second, when using one or the other approach, we need to consider the other contribution. That is, when controlling the phase using common-mode delay, the differential delay induced by a dispersive medium will add a differential delay and when controlling the phase through differential delay, the common mode delay induced by the system must be considered. This becomes especially important as the RF frequency increases since the effect of the dispersion is more notorious. Furthermore, in schemes using optical double sideband modulation, the differential delay induced by chromatic dispersion causes frequency selectivity that may significantly reduce the generated RF power [71, 72].

4.3.1. Phase Control Based on Common-Mode Delay. Phase control using common-mode delay has been extensively applied to PAAs operating at frequencies ranging from few GHz up to mm-wave frequencies. The delay can be induced changing the physical length of the path or keeping the physical length constant but changing the optical length.

TTDs using paths with different physical lengths have the advantage of operating using a constant wavelength source, which reduces the cost of the system. However, the resulting delay cannot be continuously tuned but only a set of delays can be generated. This delay discretization does not allow the implementation of adaptive antennas but it is limited to beam-switching antennas. Configurable TTDs in guided means, shown in Figure 9, require different segments of fiber or waveguides and a set of switches that select a path with the desired length. They can be implemented using serial, Figure 9(a), or parallel, Figure 9(b), architectures, as well as switching matrix, which is shown in Figure 9(c): a serial configurable TTD with 2×2 microelectromechanical system (MEMS) switches is proposed in [73]. In [74], switches based on InP are employed, but the delay elements are still fibers. A step ahead in TTD integration is presented in [75], where a 3-bit TDD using silicon-on-insulator technology is reported. Pools of configurable serial TTDs have been employed to change the phase of each element independently [30] or in a two-stage architecture that simplifies the 2D operation of the PAA [76]. In addition, it can be used either in single-wavelength systems [73] or in multiwavelength systems [77]. Serial configurable TDDs are an inexpensive approach for low number of antenna elements and applications that do not require very precise beamforming. A more precise control of the delay requires higher number of concatenated switches that will increase the insertion loss. In order to solve this issue, parallel TTDs have been proposed, as in [78], where 32 antenna elements are fed with 8-bit resolution delay using a single TDD equipped with a 3D MEMS. Nevertheless, parallel TTDs achieve better precision and scalability at the expense of more complex switches that may present significant crosstalk [79]. In addition, the high number of fibers required increases the size of the system, which can be reduced by taking advantage of modern bend-insensitive fibers [80] or integrated polymer integration [81]. Even further precision and scalability are expected from switching matrix technology [82]. TDDs in free-space optics, shown in Figure 10, are an alternative to those using guided mean. These TDDs include schemes using a diffraction mirror in combination with a rotatable MEMS [83], Figure 10(a), mechanically positioned prisms [84], Figure 10(b), and several approaches using white cells [85] and their derivatives [86], Figure 10(c). These techniques can feed a high number of antenna elements

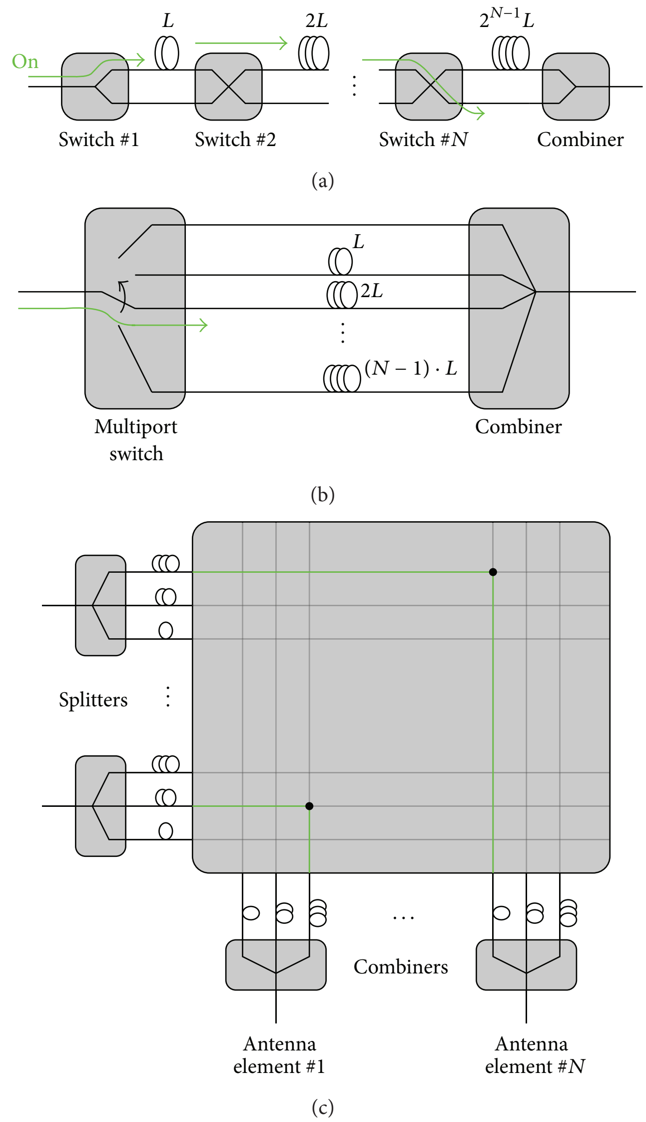

FIGURE 9: Phase control using different physical paths and guided medium: (a) serial configurable TTD and (b) parallel configurable TTD and (c) switching matrix based TTD. Green lines show the selected path.

with pretty high precision (112 antenna elements with 81 possible delays each [86]), but they are complicated to configure and very sensitive to mechanical vibrations and, therefore, they are not suitable for low-cost applications.

A time delay can also be applied changing the refractive index of the propagation path. This can be achieved in several ways as shown in Figure 11: the most common employs a tunable laser source followed by a dispersive medium. In [87], the dispersive medium is composed of a bank of standard single mode fibers/dispersion compensating fibers with different lengths, sketched in Figure 11(a). This technique is employed in [88] using a two-stage configuration to enable 2D beam steering. The size of the fiber lens can be significantly reduced by exchanging the fibers by linearly chirped fiber Bragg gratings (FBGs) [89], which is presented

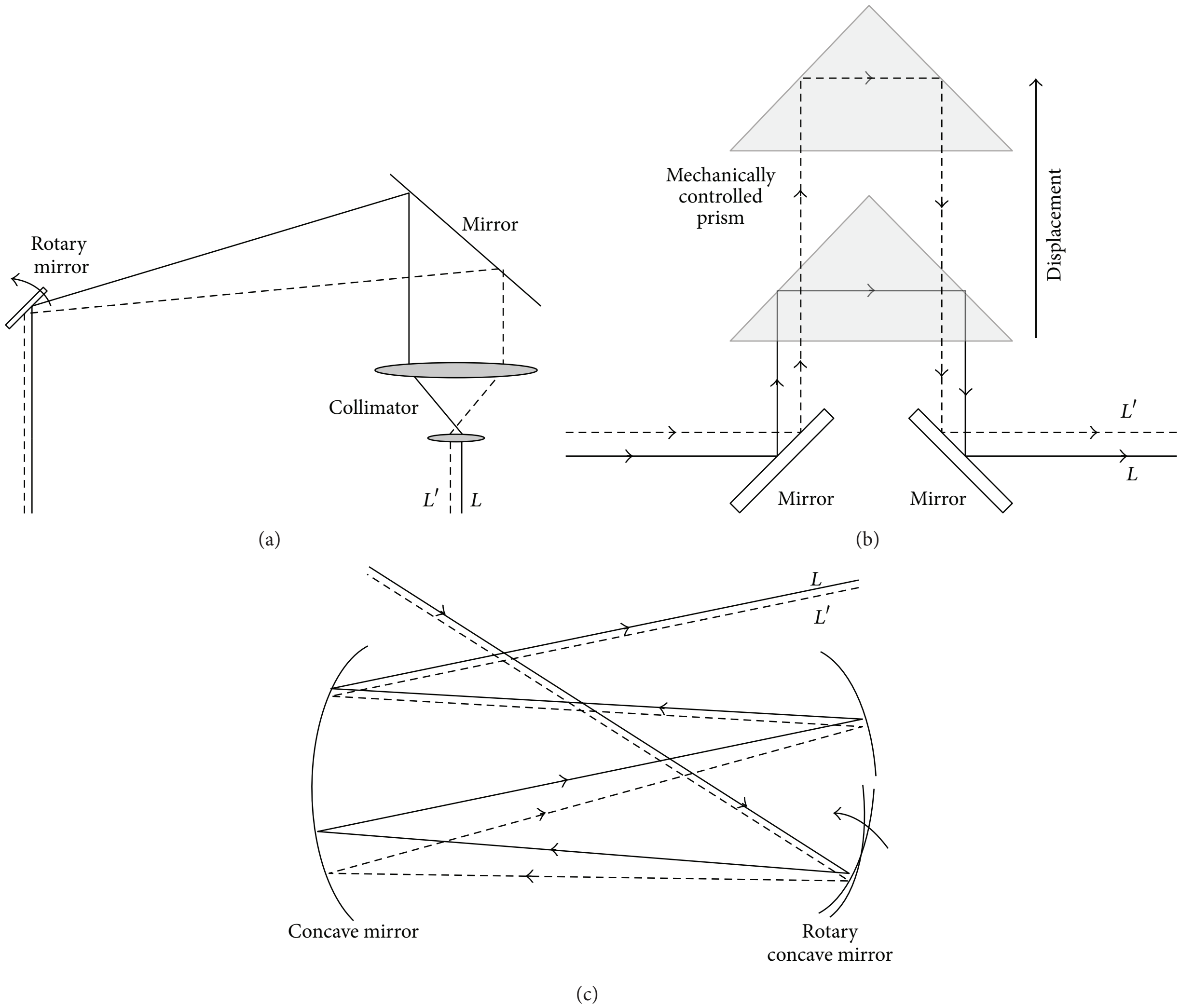

Figure 10: Phase control using different physical paths in free-space optics: (a) using a rotary mirror and a plane reflector, (b) employing a mechanically positioned prism, and (c) being based on a white cell. Solid and discontinuous time represent paths with different lengths L and L'. Arrows indicate the displacement/rotation for obtaining different lengths.

in Figure 11(b). An integrable solution to both fiber and FBG bank is a dispersion engineered material such as a photonic crystal, where dispersion slope can be tailored to meet the required shape [90]. All these techniques permit the continuous control of the phase, allowing not only beam switching but also adaptive beamforming, but they require a tunable laser. This increases the cost and requires a careful design to achieve long-term stability and avoid mode hoping [91].

4.3.2. Phase Control Based on Differential Delay. The techniques based on controlling the differential delay can be divided into those using different physical paths for the unmodulated and the modulated fields and those where both fields are propagated over the same medium but at different speed. The former requires the two components to be spatially demultiplexed, which can be achieved by means of a demultiplexer; the latter needs a dispersive medium whose dispersion slope is enough to induce the required phase shift. In both cases, the implementation of PAA at low frequencies is extremely challenging because the demultiplexing of the signal requires demultiplexers with very narrow bands or because highly dispersive material is needed. As operation frequency increases, for instance, when feeding mm-wave PAAs, the control of the differential delay becomes feasible.

Figure 12 shows a scheme where the differential delay is controlled applying a phase shift to one of the two fields. The phase shift can be performed using different technologies: in [92] the phase shift is performed employing thermoelectrical phase shifters, while in [68] the phase control is performed employing electrically controlled semiconductor devices. In both cases, the optical length of the path of one of the components is varied with a minor power penalty; however, the latter is preferable given the slower dynamics of the thermoelectrical process. In addition, this technique allows continued phase control and, with the advection of Si-based

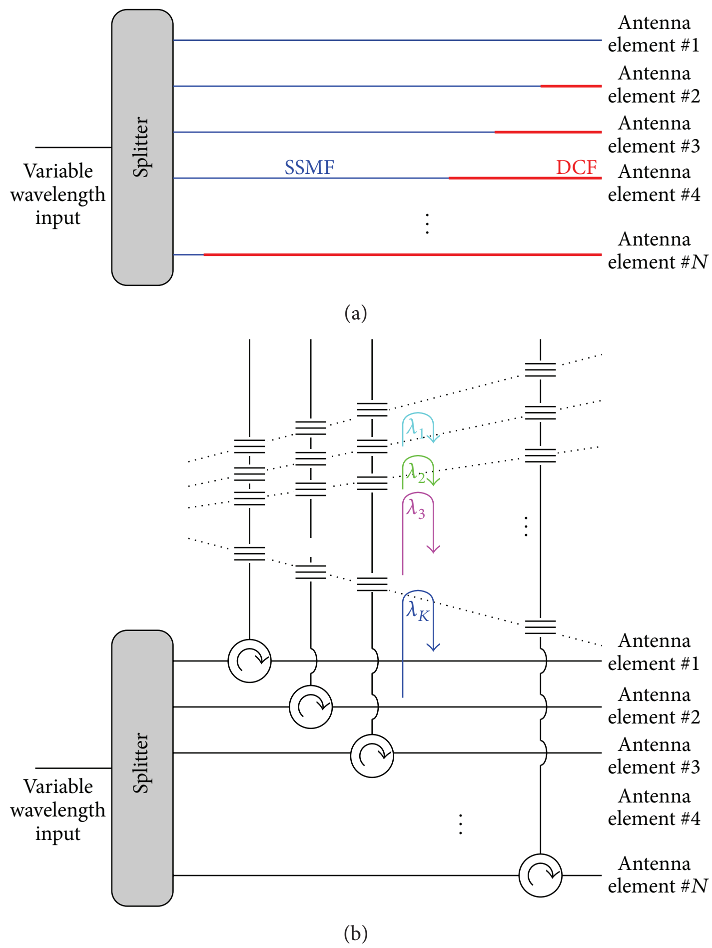

Figure 11: Phase control using (a) a bank of different standard single mode fibers (SSMF)/dispersion compensating fibers (DCF) and (b) concatenation of FBGs.

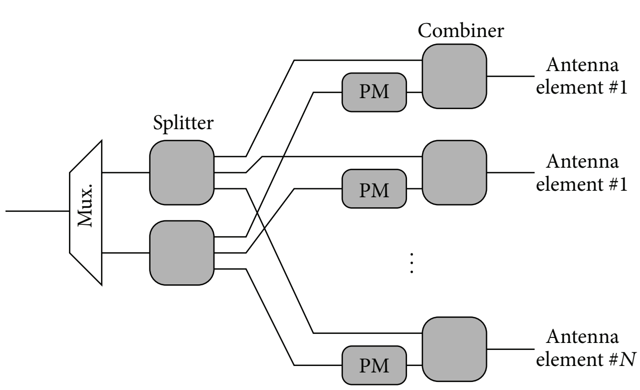

Figure 12: Phase control applying a differential delay. PM: phase modulation.

modulators [93], opens the doors to completely integrated Si-based beamformer networks.

Alternatively, the phase control can be implemented taking advantage of the frequency separation between the modulated and demodulated fields in combination with a dispersive medium, such as an optical fiber. Furthermore, a multimode source can be used to simultaneously generate the signals for the different antenna elements. The main drawback of this technique is the required tunable laser that, as already stated, increases the cost and reduces the reliability.

5. Noise in Optically Fed PAAs

Optical control of phases and amplitudes of the PAA elements presents a significantly broader bandwidth and smaller size than its electrical counterpart. However, these improvements are achieved at the expense of an elevated noise level that reduces the dynamic range of the system, deteriorating its performance. This effect has been analyzed in [94] for a single-source architecture and therefore performance of the different feeding architectures remains uncertain. In this section, we extend (9)–(12) to consider the impact of the noise on the system. We first introduce the most important noise sources that contribute to signal degradation. We then identify the two major effects of noise, that is, the time fluctuation of the total radiated power and the random amplitude and phase differences between elements that cause variation of the AF. Finally, the different architectures are evaluated in terms of the number of antenna elements and the configuration of

Table 1: Summary of the noises in optically fed PAAs.

Device	Origin	Type of noise
mm-wave generator	Spontaneous emission	Multiplicative noise
Optical amplifier	Amplified spontaneous emission	Beating noise
Photodiode	Carrier Brownian motion (thermal noise)	Additive (power independent)
	Discrete nature of photons (shot noise)	Additive (power dependent)

the mm-wave generator. In order to assess the performance, the feeding system is simulated using VPI Transmission Maker, which is capable of modeling realistically optical components such as lasers, external modulators, and PDs.

5.1. Noise Sources and Carrier-to-Noise Ratio. Noise mechanisms in optical systems differ significantly from those in electronics [55]. In particular, the power spectral density of the thermal noise drops after several THz [95] and, therefore, in optical systems passives do not induce extra noise [96]. Consequently, only the active components should be considered as noise sources. In the case of optically fed PAAs, active devices include the mm-wave generator, the optical amplifier, and the PD, whose main noise features are summarized in Table 1.

5.1.1. Noise of the Optical mm-Wave Generator. The two tones at the output of the optical mm-wave generator are corrupted by both amplitude and phase noises. However, amplitude and phase fluctuations are not independent of each other but are coupled according to the Kramers-Kronig relations, which hold in causal linear systems [66]. This coupling between the amplitude and phase noises is typically expressed in terms of the Henry factor (also known as *linewidth enhancement factor*) and depends on many design parameters such as the gain spectrum and the type of carrier confinement (bulk, multiquantum well, and quantum-dot), as well as on some operational parameters, that is, the bias current and the presence of optical injection [97]. The amplitude and phase fluctuations are a consequence of the spontaneous emission events occurring within the active gain medium. Since the spontaneous emission rate is reduced when increasing the density of photons, the power levels of the amplitude and phase noise are reduced at a higher emission power and, therefore, at a higher bias current [65].

For each wavelength, the output of the mm-wave generator acquires the form of

$$E(t) = E_{01}(t) \cdot \exp\{j[2\pi f_1 t + \phi_1(t)]\} + E_{02}(t) \cdot \exp\{j[2\pi f_2 t + \phi_2(t)]\}, \tag{21}$$

which corresponds to (9) with $m(t) = 1$ (for the sake of clarity no data transmission is assumed). The amplitudes $E_{01}(t)$ and $E_{02}(t)$ can be decomposed into a constant component, $\overline{E}_{1|2}$, and a fluctuating zero-mean term, $\Delta E_{1|2}(t)$. Consequently, $E(t)$ can be written as

$$E(t) = \left[\overline{E}_1 + \Delta E_1(t)\right] \cdot \exp\{j[2\pi f_1 t + \phi_1(t)]\} + \left[\overline{E}_2 + \Delta E_2(t)\right] \cdot \exp\{j[2\pi f_2 t + \phi_2(t)]\}. \tag{22}$$

Regarding the optical phase noise of the lasers, in most optical mm-wave generators, high correlation between $\phi_1(t)$ and $\phi_2(t)$ is forced in order to produce highly spectrally pure RF signals at the output of the PD.

5.1.2. Noise of the Optical Amplifier. When the optical signal is amplified, the amplifier adds extra noise, the so-called *amplified spontaneous emission* (ASE) noise. The amount of noise added depends on whether the amplifier is a semiconductor optical amplifier (SOA) or an erbium-doped fiber amplifier (EDFA), the gain, and the power of the incident light [55]. Then, the amplified field, $E_{\mathrm{amp}}(t)$, is expressed in terms of the amplifier power gain, G, and ASE noise, $n_{\mathrm{ASE}}(t)$:

$$E_{\mathrm{amp}}(t) = \sqrt{G} \cdot E(t) + n_{\mathrm{ASE}}(t). \tag{23}$$

The bandwidth of ASE noise is in the order of magnitude of the gain bandwidth of the active medium, which typically ranges for tens of THz-s [98]. Hence, even if at large frequency scales ASE may have some irregular spectrum, it can be considered spectrally flat (white) for the bandwidth of our signal.

The amount of ASE noise is typically given in terms of the noise figure of the optical amplifier. Typical values are 4-5 dB for EDFAs and 8-9 dB for SOAs [96].

5.1.3. Noise of the PD. In addition to the noises associated with the mm-wave generator and the optical amplifier, the PD constitutes an additional noise source. This contribution, $n_{\mathrm{PD}}(t)$, can be further divided into two components, one caused by the thermal agitation of the electrons and the other induced by the discrete nature of the electrons, which is denominated *shot noise* [99]. Both can be considered white in the bandwidth of interest but, while the power of the thermal noise does not depend on the incident light, the power of shot noise increases linearly with the power of the incident light. Consequently, shot noise is more significant at high received power levels.

Alongside the induced noise, the PDs present losses that are accounted for through the responsivity R, introduced in (10). R tends to decrease as the bandwidth of the PD increases, which may result to be problematic at high RF systems [56]. Then, the photogenerated current, $i_{\mathrm{PD}}(t)$, can be written as

$$i_{\mathrm{PD}}(t) = \frac{R \cdot \left|E_{\mathrm{amp}}(t)\right|^2}{L} + n_{\mathrm{PD}}(t), \tag{24}$$

where the power loss, L, due to passives (including the phase and amplitude control) between the amplifier and the PD has been considered.

5.1.4. Amplitude Noise in the Generated RF Signal. After introducing (21)–(23) in (24), we obtain the next expression for $i_{\mathrm{PD}}(t)$:

$$\begin{aligned} i_{\mathrm{PD}}(t) = \frac{R}{L}\Big(G\left(E_{01}^2 + E_{02}^2\right) \\ + GE_{01}(t)\,E_{02}(t)\cos\left[2\pi f_{\mathrm{mm}}t + \Delta\phi(t)\right] \\ + 2\sqrt{G}\mathrm{Re}\left\{n_{\mathrm{ASE}}(t)\,E_{01}(t)\exp j\left[2\pi f_1 t + \phi_1\right]\right\} \\ + 2\sqrt{G}\mathrm{Re}\left\{n_{\mathrm{ASE}}(t)\,E_{02}(t)\exp j\left[2\pi f_2 t + \phi_2\right]\right\} \\ + \left|n_{\mathrm{ASE}}(t)\right|^2\Big) + n_{\mathrm{PD}}(t). \end{aligned} \tag{25}$$

Since the power of the ASE noise is typically much lower than that of the amplified signal, the square of the ASE noise is generally neglected. After this assumption, ASE noise appears as a beating noise:

$$\begin{aligned} i_{\mathrm{PD}}(t) \approx \frac{R}{L}\Big(G\left(E_{01}^2 + E_{02}^2\right) \\ + GE_{01}(t)\,E_{02}(t)\cos\left[2\pi f_{\mathrm{mm}}t + \Delta\phi(t)\right] \\ + 2\sqrt{G}\mathrm{Re}\left\{n_{\mathrm{ASE}}(t)\,E_{01}(t)\exp j\left[2\pi f_1 t + \phi_1\right]\right\} \\ + 2\sqrt{G}\mathrm{Re}\left\{n_{\mathrm{ASE}}(t)\,E_{02}(t)\exp j\left[2\pi f_2 t + \phi_2\right]\right\}\Big) \\ + n_{\mathrm{PD}}(t). \end{aligned} \tag{26}$$

The RF signal is then obtained by filtering out the low-frequency components. Hence, the RF signal acquires the next form:

$$\begin{aligned} i_{\mathrm{RF}}(t) \approx \frac{R}{L}\Big(GE_{01}(t)\,E_{02}(t)\cos\left[2\pi f_{\mathrm{mm}}t + \Delta\phi(t)\right] \\ + 2\sqrt{G}\mathrm{Re}\left\{n'_{\mathrm{ASE}}(t)\,E_{01}(t)\exp j\left[2\pi f_1 t + \phi_1\right]\right\} \\ + 2\sqrt{G}\mathrm{Re}\left\{n'_{\mathrm{ASE}}(t)\,E_{02}(t)\exp j\left[2\pi f_2 t + \phi_2\right]\right\}\Big) \\ + n'_{\mathrm{PD}}(t), \end{aligned} \tag{27}$$

where $n'_{\mathrm{PD}}(t)$ and $n'_{\mathrm{ASE}}(t)$ represent the filtered signals of $n_{\mathrm{PD}}(t)$ and $n_{\mathrm{ASE}}(t)$. This expression can be written in terms of the average and fluctuating terms of the fields, giving as a result

$$\begin{aligned} i_{\mathrm{RF}}(t) \approx \frac{R}{L}\Big(G\left[\overline{E}_1 + \Delta E_1(t)\right]\cdot\left[\overline{E}_2 + \Delta E_2(t)\right] \\ \cdot\cos\left[2\pi f_{\mathrm{mm}}t + \Delta\phi(t)\right] \\ + 2\sqrt{G}\mathrm{Re}\left\{n'_{\mathrm{ASE}}(t)\left[\overline{E}_1 + \Delta E_1(t)\right]\right. \\ \left.\cdot\exp j\left[2\pi f_1 t + \phi_1\right]\right\} \\ + 2\sqrt{G}\mathrm{Re}\left\{n'_{\mathrm{ASE}}(t)\left[\overline{E}_2 + \Delta E_2(t)\right]\right. \\ \left.\cdot\exp j\left[2\pi f_2 t + \phi_2\right]\right\}\Big) + n'_{\mathrm{PD}}(t). \end{aligned} \tag{28}$$

Neglecting the beating between different fluctuations, we get

$$\begin{aligned} i_{\mathrm{RF}}(t) \approx \frac{RG}{L}\overline{E}_1\overline{E}_2\cos\left[2\pi f_{\mathrm{mm}}t + \Delta\phi(t)\right] \\ + \frac{RG}{L}\left[\Delta E_1(t)\,\overline{E}_2 + \Delta E_2(t)\,\overline{E}_1\right] \\ \cdot\cos\left[2\pi f_{\mathrm{mm}}t + \Delta\phi(t)\right] \\ + \frac{2R\sqrt{G}}{L}\mathrm{Re}\left\{n'_{\mathrm{ASE}}(t)\,\overline{E}_1\exp j\left[2\pi f_1 t + \phi_1\right]\right\} \\ + \frac{2R\sqrt{G}}{L}\mathrm{Re}\left\{n'_{\mathrm{ASE}}(t)\,\overline{E}_2\exp j\left[2\pi f_2 t + \phi_2\right]\right\} \\ + n'_{\mathrm{PD}}(t). \end{aligned} \tag{29}$$

The first term in the previous expression corresponds to the signal, whereas the others are the contributions of the different noise sources (amplitude noise of the mm-wave generator, the amplifier ASE, and the PD additive noise). As stated in Section 2.2, $\Delta\phi(t)$ is the phase difference between the two beating fields, including the phase noise of both tones. Typically, optical mm-wave generators are designed to produce highly correlated tones which results in spectrally pure RF signals [32]. *A priori*, these tones could be decorrelated if they were delayed by a different amount of time, for instance, if phase control based on differential delay is applied, causing a power penalty and spectral broadening of the generated RF signal [43]. However, according to (20), the amount of time required to phase-shift the RF signal by 2π is $2/(f_1 + f_2)$, which is much shorter than the correlation time of the source (the inverse of the linewidth) and, therefore, has a negligible effect [45]. If the signal amplitude is much higher than the amplitude of the noise signals, zero-crossing distortion can be neglected and the amplitude noise term, $n_A(t)$, acquires the form

$$\begin{aligned} n_A(t) = \frac{RG}{L}\left[\Delta E_1(t)\,\overline{E}_2 + \Delta E_2(t)\,\overline{E}_1\right] \\ + \frac{2R\sqrt{G}}{L}\mathrm{Re}\left\{n'_{\mathrm{ASE}}(t)\,\overline{E}_1\right\} \\ + \frac{2R\sqrt{G}}{L}\mathrm{Re}\left\{n'_{\mathrm{ASE}}(t)\,\overline{E}_2\right\} + n'_{\mathrm{PD}}(t). \end{aligned} \tag{30}$$

The power of the amplitude noise, P_{n_A}, can be calculated straightforward after recalling that the different noise contributions are not correlated:

$$P_{n_A} = P_{N_{\mathrm{source}}} + P_{N_{\mathrm{amp}}} + P_{N_{\mathrm{PD}}} \tag{31}$$

with

$$\begin{aligned} P_{N_{\mathrm{source}}} &= \left(\frac{RG}{L}\right)^2\overline{\left[\Delta E_1(t)\,\overline{E}_2 + \Delta E_2(t)\,\overline{E}_1\right]^2}, \\ P_{N_{\mathrm{amp}}} &= 2\left(\frac{R\sqrt{G}}{L}\right)^2\overline{n^2_{\mathrm{ASE}}(t)}\left(\overline{E}_1^2 + \overline{E}_2^2\right), \\ P_{N_{\mathrm{PD}}} &= \overline{n^2_{\mathrm{PD}}(t)}, \end{aligned} \tag{32}$$

with upper bar denoting the time average operation. Equation (32) reveals two important points: (i) All terms except $P_{N_{\mathrm{PD}}}$ decay quadratically with L and, consequently, for high L values, $P_{N_{\mathrm{PD}}}$ becomes dominant. (ii) On the other hand, for low L values, considering that G typically ranges from 20 to 30 dB, it is envisaged that $P_{N_{\mathrm{source}}}$ would be the limiting impairment. It is then useful to define the carrier-to-noise ratio (CNR) as

$$\mathrm{CNR} = \frac{P_C}{P_{n_A}} = \frac{P_C}{P_{N_{\mathrm{source}}} + P_{N_{\mathrm{amp}}} + P_{N_{\mathrm{PD}}}}, \tag{33}$$

where P_C stands for the carrier power and is given by

$$P_C = \frac{1}{2}\left(\frac{RG^2}{L}\overline{E}_1\overline{E}_2\right)^2. \tag{34}$$

5.1.5. Phase Noise in the Generated RF Signal. Even if phase correlation between optical tones is preserved, the other noise mechanisms induce phase noise on the generated RF signal. The probability density of the phase noise induced in the photogenerated current can be calculated according to this expression [45]:

$$p_\Phi(\phi) = \frac{\exp(-\gamma)}{2\pi}\left[1 + \sqrt{2\gamma}\cdot\exp\left(\gamma\cos^2\phi\right) \cdot \int_{-\infty}^{\sqrt{2\gamma}\cos(\phi)} \exp\left(\frac{-x^2}{2}\right)dx\right], \tag{35}$$

where γ is calculated as

$$\gamma = \frac{P_C}{P_{N_{\mathrm{amp}}} + P_{N_{\mathrm{PD}}}}. \tag{36}$$

It is important to note that γ does not account for the mm-wave generator noise since it does not contribute to the phase noise.

Finally, the power of the phase noise can be calculated by numerically computing the following integral:

$$P_{n_\phi} = \int_{-\infty}^{+\infty} \phi^2 p_\Phi(\phi)\,d\phi. \tag{37}$$

5.2. Effects of the Noise on the PAA Performance. The previous expressions considered a single PD and, consequently, must be extended in order to analyze the effect of noise on PAA with multiple elements. In this analysis it is important to pay special attention to the correlation among noises affecting the different antenna elements. The amount of correlation will differ for different architectures, resulting in diverse performance. According to this criterion, three cases can be differentiated.

Case 1. The noise contributions of the mm-wave generator and the optical amplifier are the same for all antenna elements. This corresponds to the architecture where a single-wavelength mm-wave generator is used to feed all the antenna elements, Figure 7(a).

Case 2. The noise contributions of the mm-wave generator are correlated but the amplifier and PD contributions are independent. This case models architectures based on multiwavelength mm-wave generators, that is, Figures 8(a) and 8(b).

Case 3. None of the noise contributions are correlated. This is the case of architectures employing different mm-wave generators, such as Figures 7(b), 8(c), and 8(d).

It is important to note that, in the case of architectures employing multiple wavelengths, the noise induced by the optical amplifier at different wavelengths is assumed to be uncorrelated because of the low coherence nature of the added noise [98].

In order to compare the performances of the different cases, the optical feeding system was simulated using VPI Transmission Maker. This software enables modeling several noise mechanisms, as well as the correlation among them. In particular, we simulated a mm-wave generator based on optical frequency doubling using an external modulator, presented in [37], that generated two highly correlated tones with 60 GHz separation. The employed laser source was simulated using the rate-equation model, whose parameters were set to match those of a standard distributed feedback (DFB) laser: a threshold current of 15 mA, a linewidth of 1 MHz, a RIN of −145 dB/Hz, and an emission power of 10 dBm at 100 mA. The amplifier noise figure and gain were set to 4 dB and 20 dB, respectively, which are typical values for an EDFA. The responsivity of the PD, R, was set to 0.6 A/W, whereas the thermal noise spectral density was set to 10^{-12} A^2/Hz.

For the sake of notation simplicity, we rename $i_{\mathrm{RF}}(t)$ in (29) to distinguish the currents generated by different PDs: from now on, $i_n(t)$ will denote the photogenerated current at RF of the nth PD.

5.2.1. Effects on the Total Radiated Power. The total radiated power can be expressed as

$$P_{\mathrm{total}}(t) = \epsilon_0 \cdot \left(\sum_{n=1}^{N} R \cdot i_n(t)\right)^2, \tag{38}$$

where, following the notation in (14), ϵ_0 accounts for the antenna efficiency and N denotes the number of elements of the PAA, while R, as in (10), represents the PD responsivity. The fluctuation of the total radiated power can be measured in terms of the normalized power standard deviation, that is, the standard deviation of the total emitted power normalized to the average total emitted power:

$$\frac{\sigma_{\Delta P}}{P_0} = \frac{\sqrt{\overline{\left(P_{\mathrm{total}} - P_0\right)^2}}}{P_0}, \tag{39}$$

where P_0 is the average power given by $P_0 = \overline{P_{\mathrm{total}}(t)}$.

Figure 13 shows the fluctuation of the normalized standard deviation of the emitted power in terms of the number of fed elements. The figure presents curves for the three

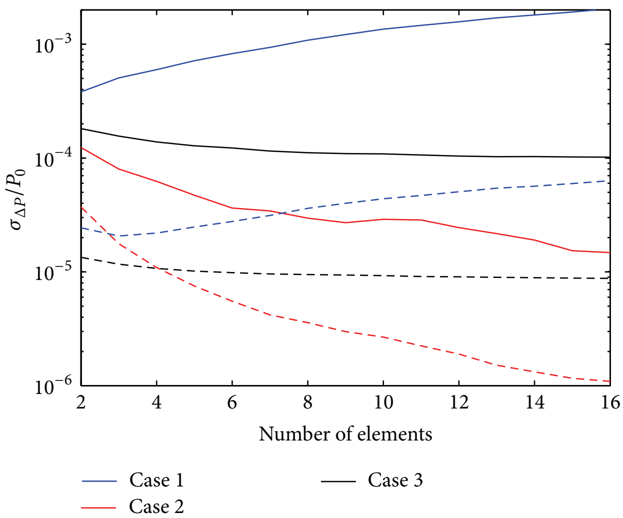

Figure 13: Normalized standard deviation of the total radiated power as a function of the number of elements for the three cases. Solid lines are for a bias current of 50 mA and discontinuous lines are for 100 mA.

cases, considering two different driving currents of the laser in the mm-wave generator, 50 mA (continuous line) and 100 mA (discontinuous line). Comparing the different cases, Case 1 presents a rising trend in the normalized standard deviation of the radiated power as the number of elements increases, whereas in Cases 2 and 3 the standard deviation drops. This reduction is explained by the partial cancellation resulting from the lack of correlation among the thermal and shot noises affecting each PD. Furthermore, in Case 2, the noise contributions of the mm-wave generator to the different antenna elements add destructively, resulting in even lower power variation. In Case 1, the standard deviation reduction due to destructive addition of noises is overcome by the reduced CNR, since the optical power is shared by the different elements. In regard to the effect of the laser bias current, in all cases, a higher bias current results in lower power fluctuation. This is an expected outcome since at higher bias currents the RIN of the source is reduced and, consequently, the noise contribution of the source is lower. Comparing the different cases, Case 1 presents the most significant improvement, which was expected since in this case the effect of the PD-induced noise is critical and, therefore, higher optical emission power considerably enhances the system performance.

5.2.2. Effects on the AF. In addition to the total radiated power fluctuation, the noise in the photogenerated currents causes deviation from the nominal amplitude and phase values of each element. This amplitude and the phase errors impact the AF term of the radiation pattern and should be studied. In order to analyze the effect of the feeding architecture, we will first study the amplitude and phase fluctuation in terms of the number of antenna elements and, afterwards, we focus on the resulting AF.

The amplitude and phase of $i_n(t)$ can be extracted from its associated analytic signal, $\tilde{i}_n(t) = i_n(t) + j \cdot \mathrm{HT}\{i_n(t)\}$, where $\mathrm{HT}\{\cdot\}$ denotes the Hilbert transform. Amplitude and phase of $i_n(t)$ are computed as

$$A_n(t) = \sqrt{\left(\mathrm{Re}\left\{\tilde{i}_n(t)\right\}\right)^2 + \left(\mathrm{Im}\left\{\tilde{i}_n(t)\right\}\right)^2},$$
$$\phi_n(t) = \mathrm{atan}\left\{\frac{\mathrm{Im}\left\{\tilde{i}_n(t)\right\}}{\mathrm{Re}\left\{\tilde{i}_n(t)\right\}}\right\}. \quad (40)$$

The time-dependent nominal values of amplitude, $A_0(t)$, and phase, $\phi_0(t)$, are given by the ensemble average of $A_n(t)$ and $\phi_n(t)$; that is,

$$A_0(t) = \frac{1}{N}\sum_{n=1}^{N} A_n(t),$$
$$\phi_0(t) = \frac{1}{N}\sum_{n=1}^{N} \phi_n(t). \quad (41)$$

The amplitude and phase deviations, $\Delta A_n(t)$ and $\Delta\phi_n(t)$, of the current generated at the nth PD are then given by

$$\Delta A_n(t) = A_n(t) - A_0(t),$$
$$\Delta\phi_n(t) = \phi_n(t) - \phi_0(t). \quad (42)$$

The amplitude error will be measured using its normalized variance, which is inversely related to the CNR; that is,

$$\frac{\sigma_A^2}{\mu_A^2} = \frac{\left\langle \Delta A_n^2(t)\right\rangle}{\left\langle A_0(t)\right\rangle^2}, \quad (43)$$

while the power of the phase error will be evaluated through its variance:

$$\sigma_\phi^2 = \left\langle \Delta\phi_n^2(t)\right\rangle. \quad (44)$$

Figures 14(a) and 14(b) show the normalized variance of the amplitude error and the variance of the phase error for the three cases in terms of the number of antenna elements, also considering two bias currents, 50 mA and 100 mA. Similar to the total radiated power, the amplitude and phase fluctuations in Case 1 degrade as the number of fed antenna elements increases, which is a consequence of the reduction of the received power. Cases 2 and 3, on the contrary, remain independent of the number of antenna elements for $N > 4$. Comparing the three cases, the best performance is achieved for Case 3, which may be attributed to the mutual cancelation, not only of the PD-induced noise but also of the noise induced by the mm-wave generator. Regarding the effect of the bias current on the amplitude and phase error, in Cases 1 and 3 significant improvements are achieved when the bias current is switched from 50 to 100 mA; on the other hand, in Case 2 a minimal improvement is observed. This minimal improvement causes the, for small number of fed antenna elements, architecture in Case 1 to outperform Case 2.

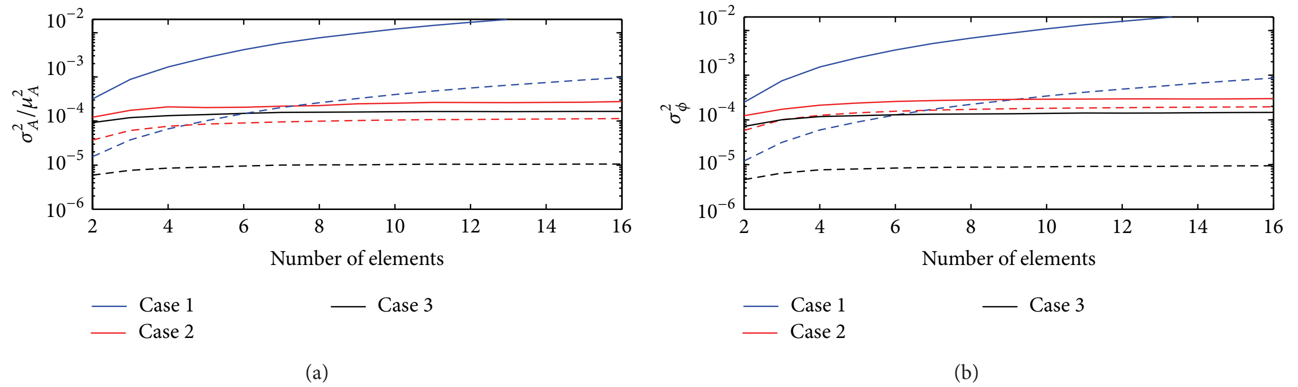

FIGURE 14: (a) Normalized variance of the amplitude error and (b) variance of the phase error as a function of the number of elements for the three cases. Solid lines are for a bias current of 50 mA and discontinuous lines are for 100 mA.

Errors in the amplitudes and phases of the feeding currents cause the AF to vary over time. In Figures 15–17 the AFs of the three cases are analyzed for a 1×8 PAA, when the bias current of the mm-wave is set to 50 mA. Subfigures labeled (a) show the *blurred* AFs, where the blurring indicates the degree of variation of the AF. Subfigures (b-d) represent the time evolution of $G_{\max}$ and the direction of maximum radiation, $\theta_{\max}$, respectively, whereas subfigures (c-e) show the histogram of these quantities. Looking at the AFs, it is clear that their variations are more notorious close to the zeros, in particular for Case 1. Comparing the different cases, Cases 2 and 3 present similar performance in terms of time variation in $G_{\max}$ and $\theta_{\max}$, while Case 1 reveals a significantly higher variation in both figures of merit. These results are in agreement with the curves presented in Figure 14, where Cases 2 and 3 present almost the same phase and amplitude variation, whose power level is much lower than that of Case 1.

In order to analyze the effect of the number of fed elements, we focus on Case 1 since, in Cases 2 and 3, the variances of amplitude and phase errors remain almost constant. In Figures 18–20, the same figures of merit as in Figures 15–17 are shown, but only for Case 1 and different numbers of elements: Figure 18 is for 1×4 PAA elements, Figure 19 is for 1×8 PAA, and Figure 20 is for 1×16 PAA. These figures reveal that variations of $G_{\max}$ rise with the number of elements, while the variation of $\theta_{\max}$ reduces. The increment in the variation of $G_{\max}$ seems logical from Figure 14; however, from the same figure, we might think that variation in $\theta_{\max}$ should also increase, which contradicts the obtained results. This discrepancy can be explained by noting that for higher number of antenna elements, the shape of the main lobe of the AF narrows. This further causes that the direction of maximum radiation to be more clearly defined.

The analysis of the impact of the noise on PAA performance drives an important conclusion: effectively, PAAs operating at mm-wave frequencies can be optically fed, at least for a moderate number of elements. We also conclude that the chosen architecture has a critical effect on the amplitude and phase errors of the antenna elements; thus, feeding architecture based on multiple mm-wave generators is the optimum solution. Nevertheless, a lower cost approach, such as an architecture employing a single mm-wave generator, is feasible at the expense of higher variation on the total radiated power and AF, which requires higher transmission power and complicates spatial multiplexing and interference avoidance.

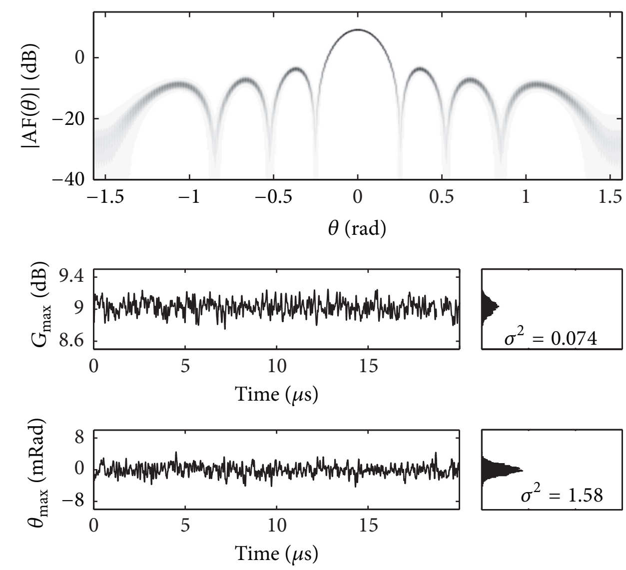

FIGURE 15: Case 1. 1×8 PAA: (a) AF, (b) $G_{\max}$, and (c) its histogram. (d) Direction of maximum radiation and (e) its histogram.

6. Research Opportunities

Despite the great effort dedicated to the development of the efficient optical control schemes, some issues remain unresolved, as follows.

(i) Integration Using Silicon Photonics. Silicon photonics enables the integration of a huge number of optical variable attenuators/phase shifters, alongside the complementary metal-oxide-semiconductor (CMOS) control circuitry, in a reduced footprint chip. Nevertheless, silicon-based devices

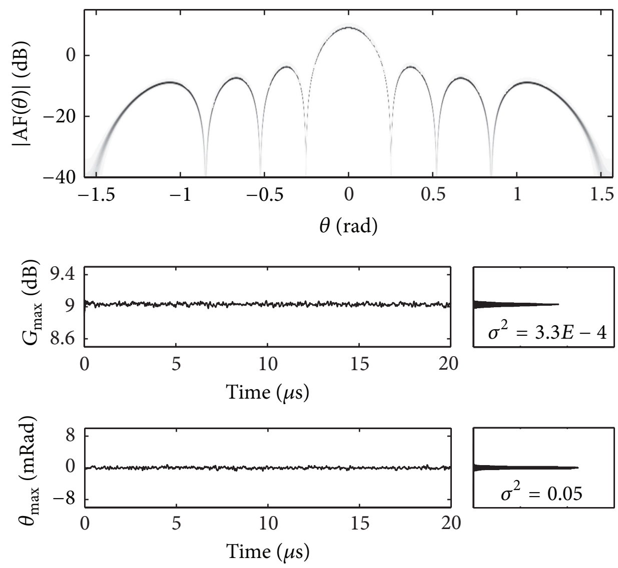

Figure 16: Case 2. 1×8 PAA: (a) AF, (b) G_{max}, and (c) its histogram. (d) Direction of maximum radiation and (e) its histogram.

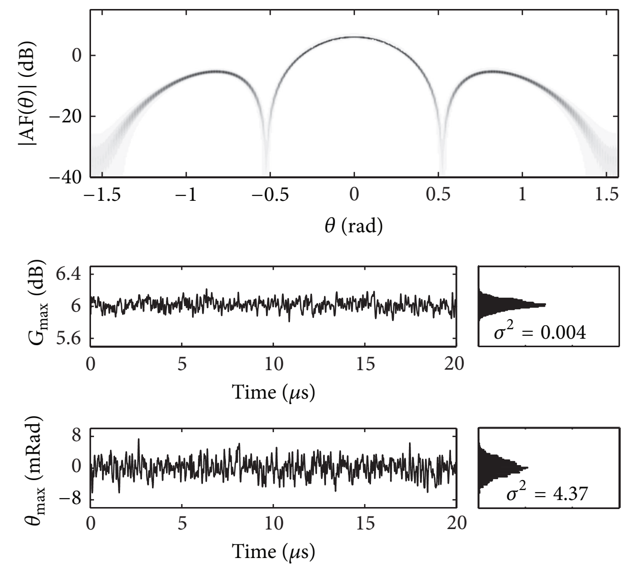

Figure 18: Case 1. 1×4 PAA: (a) AF, (b) G_{max}, and (c) its histogram. (d) Direction of maximum radiation and (e) its histogram.

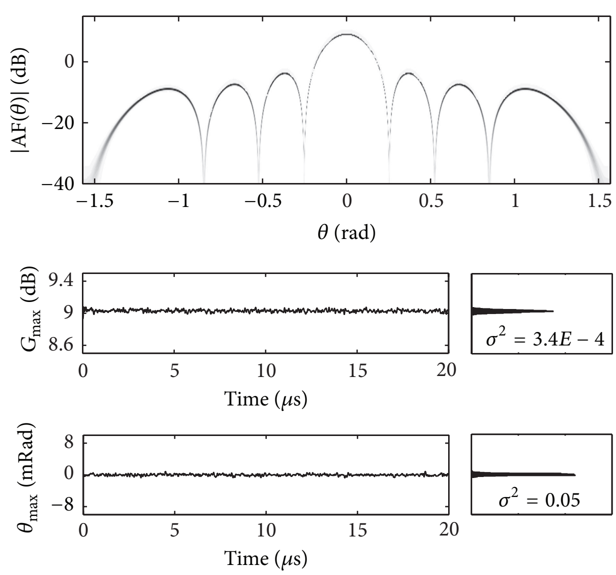

Figure 17: Case 3. 1×8 PAA: (a) AF, (b) G_{max}, and (c) its histogram. (d) Direction of maximum radiation and (e) its histogram.

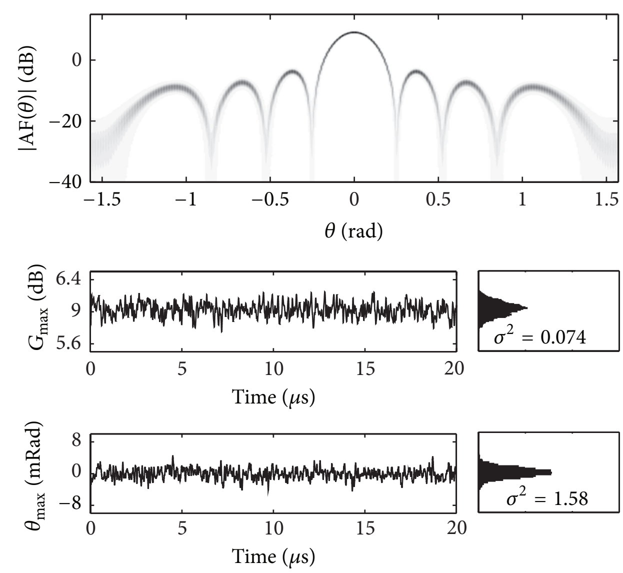

Figure 19: Case 1. 1×8 PAA: (a) AF, (b) G_{max}, and (c) its histogram. (d) Direction of maximum radiation and (e) its histogram.

still present significant insertion losses, which may become a limiting impairment hindering their implementation.

(ii) Balanced PDs. Most of the reported feeding architectures are based on unbalanced photodetection. Balanced photodetection avoids the requirement for filtering out the low-frequency components and improves the dynamic range of the system [100]. In this case, the integration of the antenna with balanced photodetectors should be analyzed.

(iii) Preamplified PDs. Since the radiated power depends on the output power of the PDs, it is important that the incident optical power be high enough. This may be difficult in PAAs with a high number of elements. In the case of multiwavelength mm-wave generators, the total power is divided among all the channels, so the power per channel is expected to be relatively low, while when a single-channel mm-wave generator is used, splitting loss increases as the number of antenna elements to be fed. In both cases, an optical amplifier preceding the PD will increase the maximum number of antenna elements. This preamplifier may be built using semiconductor technology, making its integration with the PD feasible.

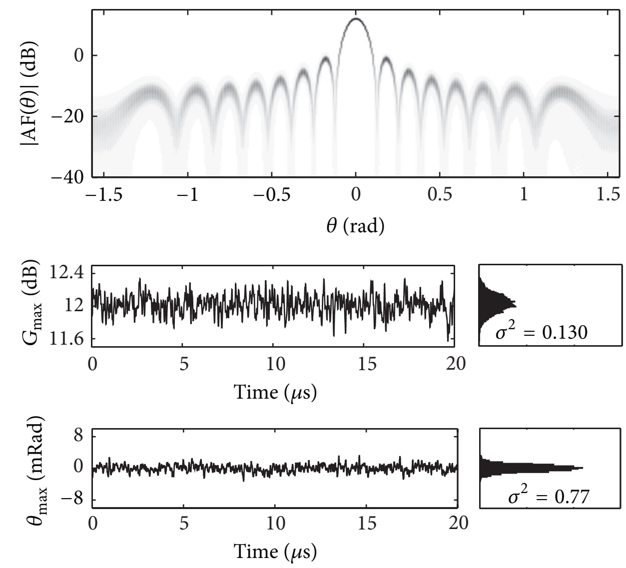

FIGURE 20: Case 1. 1×16 PAA: (a) AF, (b) G_{max}, and (c) its histogram. (d) Direction of maximum radiation and (e) its histogram.

7. Conclusions

Optical phase and amplitude control of mm-wave PAA elements overcomes the bandwidth limitation of its electrical counterpart. However, optical feeding still poses some challenges such as the integration of antenna elements with the high-speed PD, the efficient implementation of the phase and amplitude control, and the noise induced on the generated feeding signals, which further results in temporal emitted power and radiation pattern fluctuations. In this paper, we have discussed these challenges and listed the most prominent techniques in the literature, presenting their advantages and disadvantages. In addition, we analyzed the impact of the noise on both the emission power fluctuation and radiation patter variation considering the correlation among the noises affecting the different antenna elements. Thus, simulation results revealed that the chosen beamforming architecture has a critical impact on the PAA performance. This work is intended to be a guideline for both antenna engineers interested in optical phase and amplitude control techniques and optical engineers keen on applying photonics to the feeding of mm-wave PAA. We have included a list of tentative research opportunities that, to our criterion, deserve further study.

Conflict of Interests

The authors declare that there is no conflict of interests regarding the publication of this paper.

References

[1] Cisco Systems, "Cisco visual networking index: forecast and methodology, 2012–2017," Tech. Rep., Cisco Systems, San Francisco, Calif, USA, 2013.

[2] Cisco, "Cisco visual networking index: mobile data traffic forecast update," Tech. Rep., Cisco, 2014.

[3] T. Rappaport, W. Roh, and K. Cheun, "Mobile's millimeter-wave makeover," *IEEE Spectrum*, vol. 51, no. 9, pp. 34–58, 2014.

[4] C. J. Hansen, "WiGiG: multi-gigabit wireless communications in the 60 GHz band," *IEEE Wireless Communications*, vol. 18, no. 6, pp. 6–7, 2011.

[5] I. WPAN, Task Group 3c (TG3c) MillimeterWave Alternative PHY, http://ieee802.org/15/pub/TG3c.html.

[6] ECMA International, "High rate 60 GHz PHY, MAC and PALs," Standard ECMA-387, ECMA International, 2010.

[7] Z. Pi and F. Khan, "An introduction to millimeter-wave mobile broadband systems," *IEEE Communications Magazine*, vol. 49, no. 6, pp. 101–107, 2011.

[8] A. Lebedev, X. Pang, J. J. Vegas Olmos et al., "Feasibility study and experimental verification of simplified fiber-supported 60-GHz picocell mobile backhaul links," *IEEE Photonics Journal*, vol. 5, no. 4, pp. 1–14, 2013.

[9] T. Rappaport, S. Sun, R. Mayzus et al., "Millimeter wave mobile communications for 5G cellular: it will work!," *IEEE Access*, vol. 1, pp. 335–349, 2013.

[10] C. Dehos, J. González, A. de Domenico, D. Ktéenas, and L. Dussopt, "Millimeter-wave access and backhauling: the solution to the exponential data traffic increase in 5G mobile communications systems?" *IEEE Communications Magazine*, vol. 52, no. 9, pp. 88–95, 2014.

[11] R. C. Daniels and R. W. Heath Jr., "60 GHz wireless communications: emerging requirements and design recommendations," *IEEE Vehicular Technology Magazine*, vol. 2, no. 3, pp. 41–50, 2007.

[12] F. Giannetti, M. Luise, and R. Reggiannini, "Mobile and personal communications in the 60 GHz band: a survey," *Wireless Personal Communications*, vol. 10, no. 2, pp. 207–243, 1999.

[13] S. Hur, T. Kim, D. J. Love, J. V. Krogmeier, T. A. Thomas, and A. Ghosh, "Millimeter wave beamforming for wireless backhaul and access in small cell networks," *IEEE Transactions on Communications*, vol. 61, no. 10, pp. 4391–4403, 2013.

[14] W. Roh, J.-Y. Seol, J. Park et al., "Millimeter-wave beamforming as an enabling technology for 5G cellular communications: theoretical feasibility and prototype results," *IEEE Communications Magazine*, vol. 52, no. 2, pp. 106–113, 2014.

[15] L. Wang, M. Elkashlan, T. Q. Duong, and R. W. Heath, "Secure communication in cellular networks: the benefits of millimeter wave mobile broadband," in *Proceedings of the IEEE 15th International Workshop on Signal Processing Advances in Wireless Communications (SPAWC '14)*, pp. 115–119, Toronto, Canada, June 2014.

[16] L. C. Godara, "Applications of antenna arrays to mobile communications, part I: performance improvement, feasibility, and system considerations," *Proceedings of the IEEE*, vol. 85, no. 7, pp. 1031–1060, 1997.

[17] C. Balanis, *Antenna Theory: Analysis and Design*, John Wiley and Sons, 3rd edition, 2005.

[18] M. Y. Frankel and R. D. Esman, "True time-delay fiber-optic control of an ultrawideband array transmitter/receiver with multibeam capability," *IEEE Transactions on Microwave Theory and Techniques*, vol. 43, no. 9, pp. 2387–2394, 1995.

[19] W.-Q. Che, E. K.-N. Yung, K. Wu, and X.-D. Nie, "Design investigation on millimeter-wave ferrite phase shifter in substrate integrated waveguide," *Progress in Electromagnetics Research*, vol. 45, pp. 263–275, 2004.

[20] D. Liu, B. Gaucher, U. Pfeiffer, and J. Grzyb, *Millimeter-Wave Technologies*, John Wiley and Sons, 2009.

[21] A. J. Seeds, "Microwave photonics," *IEEE Transactions on Microwave Theory and Techniques*, vol. 50, no. 3, pp. 877–887, 2002.

[22] J. Yao, "Microwave photonics," *Journal of Lightwave Technology*, vol. 27, no. 3, pp. 314–335, 2009.

[23] M. F. Jahromi, *Optical and microwave beamforming for phased array antennas [Ph.D. thesis]*, University of Waterloo, 2008.

[24] R. Mailloux, *Phased Array Antenna Handbook*, Artech House, 2nd edition, 2005.

[25] H. Zmuda and E. N. Toughlian, *Photonic Aspects of Modern Radar*, Artech House, 1994.

[26] S. Saunders and A. Aragón-Zavala, *Antennas and Propagation for Wireless Communication Systems*, Wiley & Sons, 2nd edition, 2005.

[27] K. Chang, R. A. York, P. S. Hall, and T. Itoh, "Active integrated antennas," *IEEE Transactions on Microwave Theory and Techniques*, vol. 50, no. 3, pp. 937–944, 2002.

[28] H. Singh, H. L. Sneha, and R. M. Jha, "Mutual coupling in phased arrays: a review," *International Journal of Antennas and Propagation*, vol. 2013, Article ID 348123, 23 pages, 2013.

[29] C. A. Balanis, Ed., *Modern Antenna Handbook*, John Wiley & Sons, Hoboken, NJ, USA, 2008.

[30] M. A. Piqueras, G. Grosskopf, B. Vidal et al., "Optically beamformed beam-switched adaptive antennas for fixed and mobile broad-band wireless access networks," *IEEE Transactions on Microwave Theory and Techniques*, vol. 54, no. 2, pp. 887–899, 2006.

[31] J. Beas, G. Castanon, I. Aldaya, A. Aragon-Zavala, and G. Campuzano, "Millimeter-wave frequency radio over fiber systems: a survey," *IEEE Communications Surveys and Tutorials*, vol. 15, no. 4, pp. 1593–1619, 2013.

[32] I. Aldaya, J. Beas, G. Castañón, G. Campuzano, and A. Aragón-Zavala, "A survey of key-enabling components for remote millimetric wave generation in radio over fiber networks," *Optics and Laser Technology*, vol. 49, pp. 213–226, 2013.

[33] P. Hartmann, X. Qian, A. Wonfor, R. V. Penty, and I. H. White, "1–20 GHz directly modulated radio over MMF link," in *Proceedings of the International Topical Meeting on Microwave Photonics (MWP '05)*, pp. 95–98, October 2005.

[34] L. Goldberg, H. F. Taylor, J. F. Weller, and D. M. Bloom, "Microwave signal generation with injection-locked laser diodes," *Electronics Letters*, vol. 19, no. 13, pp. 491–493, 1983.

[35] R. P. Braun and G. Grosskopf, "Optical millimeter-wave systems for broadband mobile communications, devices and techniques," in *Proceedings of International Zurich Seminar on Broadband Communications. Accessing, Transmission, Networking*, pp. 51–58, Zurich, Switzerland, 1998.

[36] D. Parekh, W. Yang, A. Ng'Oma et al., "Multi-Gbps ASK and QPSK-modulated 60 GHz RoF link using an optically injection locked VCSEL," in *Proceedings of the Optical Fiber Communication/National Fiber Optic Engineers Conference (OFC/NFOEC '10)*, pp. 1–3, 2010.

[37] Z. Jia, J. Yu, A. Chowdhury, G. Ellinas, and G.-K. Chang, "Simultaneous generation of independent wired and wireless services using a single modulator in millimeter-wave-band radio-over-fiber systems," *IEEE Photonics Technology Letters*, vol. 19, no. 20, pp. 1691–1693, 2007.

[38] S. Makino, K. Shinoda, T. Kitatani et al., "High-speed electroabsorption modulator integrated DFB laser for 40 Gbps and 100 Gbps application," in *Proceedings of the IEEE International Conference on Indium Phosphide & Related Materials (IPRM '09)*, pp. 362–366, IEEE, Newport Beach, Calif, USA, May 2009.

[39] M. Huchard, P. Chanclou, B. Charbonnier et al., "60 GHz radio signal up-conversion and transport using a directly modulated mode-locked laser," in *Proceedings of the IEEE International Topical Meeting on Microwave Photonics*, pp. 333–335, Gold Coast, Australia, October 2008.

[40] M. Attygalle, C. Lim, and A. Nirmalathas, "Dispersion-tolerant multiple WDM channel millimeter-wave signal generation using a single monolithic mode-locked semiconductor laser," *Journal of Lightwave Technology*, vol. 23, no. 1, pp. 295–303, 2005.

[41] K. Mori, K. Sato, H. Takara, and T. Ohara, "Supercontinuum lightwave source generating 50 GHz spaced optical ITU grid seamlessly over S-, C- and L-bands," *IEE Electronics Letters*, vol. 39, no. 6, pp. 544–546, 2003.

[42] C.-T. Lin, J. Chen, W.-J. Jiang et al., "Ultra-high data-rate 60 GHz radio-over-fiber systems employing optical frequency multiplication and adaptive OFDM formats," in *Proceedings of the Optical Fiber Communication Conference and Exposition and the National Fiber Optic Engineers Conference (OFC/NFOEC '11)*, pp. 1–3, March 2011.

[43] G. H. Smith, D. Novak, and Z. Ahmed, "Overcoming chromatic-dispersion effects in fiber-wireless systems incorporating external modulators," *IEEE Transactions on Microwave Theory and Techniques*, vol. 45, no. 8, pp. 1410–1415, 1997.

[44] P. B. Gallion and G. Debarge, "Quantum phase noise and field correlationin single frequency semiconductor laser systems," *IEEE Journal of Quantum Electronics*, vol. 20, no. 4, pp. 343–349, 1984.

[45] U. Gliese, S. Norskov, and T. N. Nielsen, "Chromatic dispersion in fiber-optic microwave and millimeter-wave links," *IEEE Transactions on Microwave Theory and Techniques*, vol. 44, no. 10, pp. 1716–1724, 1996.

[46] A. Ng'oma and M. Sauer, "Radio-over-fiber systems for multi-Gbps wireless communication," in *Proceedings of the Asia Communications and Photonics Conference and Exhibition (ACP '09)*, pp. 1–9, November 2009.

[47] L. Goldberg, R. D. Esman, and K. J. Williams, "Generation and control of microwave signals by optical techniques," *IEE Proceedings J: Optoelectronics*, vol. 139, no. 4, pp. 288–295, 1992.

[48] R. Masood and S. A. Mohsin, "Characterization of a coplanar waveguide open stub-based discontinuity for mmics and filter applications," *International Journal of Antennas and Propagation*, vol. 2012, Article ID 423706, 9 pages, 2012.

[49] H. Vettikalladi, W. T. Sethi, and M. A. Alkanhal, "High gain and high efficient stacked antenna array with integrated horn for 60 GHz communication systems," *International Journal of Antennas and Propagation*, vol. 2014, Article ID 418056, 8 pages, 2014.

[50] Y. Liu, L.-M. Si, M. Wei et al., "Some recent developments of microstrip antenna," *International Journal of Antennas and Propagation*, vol. 2012, Article ID 428284, 10 pages, 2012.

[51] A. Enayati, W. De Raedt, and G. A. E. Vandenbosch, "Antenna-in-package solution for millimeter-wave applications: slotted-patch in a multilayer PCB," in *Proceedings of the IEEE International Symposium on Antennas and Propagation and USNC-URSI National Radio Science Meeting (APSURSI '12)*, pp. 1–2, July 2012.

[52] B. Cheng, H. Xue, C. Xue et al., "Silicon-based long wavelength photodetectors," in *Optoelectronic Materials and Devices IV*, vol. 7631 of *Proceedings of SPIE*, December 2009.

[53] M. W. Geis, S. J. Spector, M. E. Grein et al., "CMOS-compatible all-Si high-speed waveguide photodiodes with high responsivity in near-infrared communication band," *IEEE Photonics Technology Letters*, vol. 19, no. 3, pp. 152–154, 2007.

[54] E. Sackinger, *Broadband Circuits for Optical Fiber Communication*, John Wiley & Sons, 2005.

[55] G. P. Agrawal, *Fiber-Optic Communication Systems*, John Wiley & Sons, 2002.

[56] H. Ito, S. Kodama, Y. Muramoto, T. Furuta, T. Nagatsuma, and T. Ishibashi, "High-speed and high-output InP-InGaAs unitraveling-carrier photodiodes," *IEEE Journal on Selected Topics in Quantum Electronics*, vol. 10, no. 4, pp. 709–727, 2004.

[57] H. Ito, T. Yoshimatsu, H. Yamamoto, and T. Ishibashi, "Broadband photonic terahertz-wave emitter integrating UTC-PD and novel planar antenna," in *Terahertz Physics, Devices, and Systems VII: Advanced Applications in Industry and Defense*, vol. 8716 of *Proceedings of SPIE*, April 2013.

[58] H. Ito, T. Nagatsuma, A. Hirata et al., "High-power photonic millimetre wave generation at 100 GHz using matching-circuit-integrated uni-travelling-carrier photodiodes," *IEE Proceedings: Optoelectronics*, vol. 150, no. 2, pp. 138–142, 2003.

[59] C. C. Renaud, M. Robertson, D. Rogers et al., "A high responsivity, broadband waveguide uni-travelling carrier photodiode," in *Millimeter-Wave and Terahertz Photonics*, vol. 6194 of *Proceedings of SPIE*, Strasbourg, France, April 2006.

[60] H. F. Pues and A. R. van de Capelle, "Impedance-matching technique for increasing the bandwidth of microstrip antennas," *IEEE Transactions on Antennas and Propagation*, vol. 37, no. 11, pp. 1345–1354, 1989.

[61] K. Li, T. Matsui, and M. Izutsu, "Photonic antennas and its application to radio-over-fiber wireless communication systems," *Journal of the National Institute of Information and Communications Technology*, vol. 51, no. 1-2, pp. 141–149, 2004.

[62] L. Morgan and H. Andersson, "An efficient beamforming method using a combination of analog true time and digital delay," in *Proceedings of the IEEE Radar Conference*, pp. 260–265, April 2002.

[63] H. Aliakbarian, V. Volski, E. van der Westhuizen, R. Wolhuter, and G. A. E. Vandenbosch, "Analogue versus digital for baseband beam steerable array used for LEO satellite applications," in *Proceedings of the 4th European Conference on Antennas and Propagation (EuCAP '10)*, pp. 1–4, IEEE, Barcelona, Spain, April 2010.

[64] F. van Vliet, "Photonic beamforming for phased-array radar," in *Proceedings of the International Union of Radio Science*, vol. 1–4, Maastricht, The Netherlands, August 2002.

[65] J. Buus, *Single Frequency Semiconductor Lasers*, vol. TT5, SPIE Optical Engineering Press, Bellingham, Wash, USA, 1st edition, 1990.

[66] J. Carroll, J. Whiteway, and D. Plumb, *Distributed Feedback Semiconductor Lasers*, IEE/SPIE Optical Engineering Press, 1998.

[67] W. S. Birkmayer and M. J. Wale, "Proof-of-concept model of a coherent optical beam-forming network," *IEE proceedings*, vol. 139, no. 4, pp. 301–304, 1992.

[68] J. Stulemeijer, F. E. van Vliet, K. W. Benoist, D. H. Maat, and M. K. Smit, "Compact photonic integrated phase and amplitude controller for phased-array antennas," *IEEE Photonics Technology Letters*, vol. 11, no. 1, pp. 122–124, 1999.

[69] H. Li, T. Huang, C. Ke, S. Fu, P. P. Shum, and D. Liu, "Photonic generation of frequency-quadrupled microwave signal with tunable phase shift," *IEEE Photonics Technology Letters*, vol. 26, no. 3, pp. 220–223, 2014.

[70] M. Tamburrini, M. Parent, L. Goldberg, and D. Stillwell, "Optical feed for a phased array microwave antenna," *Electronics Letters*, vol. 23, no. 13, pp. 680–681, 1987.

[71] M. Oishi, H. Matsuno, K. Nishimura, and S. Akiba, "Experimental study of chromatic dispersion effects on antenna beam forming by RF over fiber," in *Proceedings of the IEEE International Topical Meeting on Microwave Photonics (MWP '12)*, pp. 140–143, September 2012.

[72] M. Oishi, Y. Nishikawa, S. Akiba, J. Hirokawa, and M. Ando, "2-dimensional beam steering by 2×3 photonic antenna using millimeter-wave radio over fiber," in *Proceedings of the IEEE International Topical Meeting on Microwave Photonics (MWP '13)*, pp. 130–133, October 2013.

[73] J.-D. Shin, B.-S. Lee, and B.-G. Kim, "Optical true time-delay feeder for X-band phased array antennas composed of 2×2 optical MEMS switches and fiber delay lines," *IEEE Photonics Technology Letters*, vol. 16, no. 5, pp. 1364–1366, 2004.

[74] F. M. Soares, F. Karouta, E. J. Geluk, J. H. C. van Zantvoort, H. de Waardt, and M. K. Smit, "Integrated InP-based true time delay with fiber mode adapter for beamforming," in *Proceedings of the 210th ECS Meeting*, Cancun, Mexico, October-November 2006.

[75] J. Xie, L. Zhou, Z. Li, J. Wang, and J. Chen, "Seven-bit reconfigurable optical true time delay line based on silicon integration," *Optics Express*, vol. 22, no. 19, pp. 22707–22715, 2014.

[76] B.-M. Jung, J.-D. Shin, and B.-G. Kim, "Optical true time-delay for two-dimensional X-band phased array antennas," *IEEE Photonics Technology Letters*, vol. 19, no. 12, pp. 877–879, 2007.

[77] D. T. K. Tong and M. C. Wu, "Multiwavelength optically controlled phased-array antennas," *IEEE Transactions on Microwave Theory and Techniques*, vol. 46, no. 1, pp. 108–115, 1998.

[78] V. Kaman, X. Zheng, R. J. Helkey, C. Pusarla, and J. E. Bowers, "A 32-element 8-bit photonic true-time-delay system based on a 288×288 3-D MEMS optical switch," *IEEE Photonics Technology Letters*, vol. 15, no. 6, pp. 849–851, 2003.

[79] T.-W. Yeow, K. L. Eddie, and A. Goldenberg, "MEMS optical switches," *IEEE Communications Magazine*, vol. 39, no. 11, pp. 158–163, 2001.

[80] M.-J. Li, P. Tandon, D. C. Bookbinder et al., "Ultra-low bending loss single-mode fiber for FTTH," *Journal of Lightwave Technology*, vol. 27, no. 3, pp. 376–382, 2009.

[81] C. Chen, Y. Yi, F. Wang, Y. Yan, X. Sun, and D. Zhang, "Ultra-long compact optical polymeric array waveguide true-time-delay line devices," *IEEE Journal of Quantum Electronics*, vol. 46, no. 5, pp. 754–761, 2010.

[82] A. Capozzoli, C. Curcio, and G. D'Elia, "The design of an optical time steered antenna based on a new integrated true time delay unit," *Progress in Electromagnetics Research*, vol. 140, pp. 681–717, 2013.

[83] R. T. Schermer, F. Bucholtz, and C. A. Villarruel, "Continuously-tunable microwave photonic true-time-delay based on a fiber-coupled beam deflector and diffraction grating," *Optics Express*, vol. 19, no. 6, pp. 5371–5378, 2011.

[84] D. Dolfi, P. Joffre, J. Antoine, J.-P. Huignard, D. Philippet, and P. Granger, "Experimental demonstration of a phased-array antenna optically controlled with phase and time delays," *Applied Optics*, vol. 35, no. 26, pp. 5293–5300, 1996.

[85] A. Rader and B. L. Anderson, "Demonstration of a linear optical true-time delay device by use of a microelectromechanical mirror array," *Applied Optics*, vol. 42, no. 8, pp. 1409–1416, 2003.

[86] B. L. Anderson, J. G. Ho, W. D. Cowan et al., "Hardware demonstration of extremely compact optical true time delay device for wideband electronically steered antennas," *Journal of Lightwave Technology*, vol. 29, no. 9, Article ID 5727896, pp. 1343–1353, 2011.

[87] R. D. Esman, M. Y. Frankel, J. L. Dexter et al., "Fiber-optic prism true time-delay antenna feed," *IEEE Photonics Technology Letters*, vol. 5, no. 11, pp. 1347–1349, 1993.

[88] P. Wu, S. Tang, and D. E. Raible, "A prototype high-speed optically-steered X-band phased array antenna," *Optics Express*, vol. 21, no. 26, pp. 32599–32604, 2013.

[89] H. Zmuda, R. A. Soref, P. Payson, S. Johns, and E. N. Toughlian, "Photonic beamformer for phased array antennas using a fiber grating prism," *IEEE Photonics Technology Letters*, vol. 9, no. 2, pp. 241–243, 1997.

[90] H. Subbaraman, M. Y. Chen, and R. T. Chen, "Photonic crystal fiber-based true-time-delay beamformer for multiple RF beam transmission and reception of an X-band phased-array antenna," *Journal of Lightwave Technology*, vol. 26, no. 15, pp. 2803–2809, 2008.

[91] P. Matthews and P. Biernacki, "Recent progress in dispersion-based photonic beamforming," in *Technical Digest. International Topical Meeting on Microwave Photonics (MWP '00)*, pp. 1–4, Oxford, UK, 2000.

[92] G. Grosskopf, B. Kuhlow, R. Eggemann, G. Przyrembel, and D. Rohde, "Photonic beam-forming for millimeter-wave mobile communications," in *Proceedings of the IEEE LEOS Annual Meeting Conference Proceedings*, vol. 2, pp. 859–860, October 2003.

[93] R. Soref, "The past, present, and future of silicon photonics," *IEEE Journal on Selected Topics in Quantum Electronics*, vol. 12, no. 6, pp. 1678–1687, 2006.

[94] T. Landolsi, L. S. Tamil, and W. P. Osborne, "Effect of noise in optically-fed phased array antennas for CDMA wireless networks," in *Proceedings of the IEEE International Conference on Personal Wireless Communications*, pp. 244–247, December 1997.

[95] D. Abbott, B. R. Davis, N. J. Phillips, and K. Eshraghian, "Simple derivation of the thermal noise formula using window-limited fourier transforms and other conundrums," *IEEE Transactions on Education*, vol. 39, no. 1, pp. 1–13, 1996.

[96] R. Ramaswami and K. N. Sivarajan, *Optical Networks: A practical Perspective*, Morgan Kaufmann, Boston, Mass, USA, 2002.

[97] L. A. Coldren and S. W. Corzine, *Diode Lasers and Photonic Integrated Circuits*, John Wiley & Sons, 1995.

[98] P. M. Becker, A. A. Olsson, and J. R. Simpson, *Erbium-Doped Fiber Amplifiers: Fundamentals and Technology*, Academic Press, New York, NY, USA, 1999.

[99] S. B. Alenxander, *Optical Communication Receiver Design*, vol. TT22, SPIE Optical Engineering Press, 1997.

[100] L. Zhuang, A. Meijerink, C. G. H. Roeloffzen et al., "Novel ring resonator-based optical beamformer for broadband phased array receive antennas," in *Proceedings of the 21st Annual Meeting of the IEEE Lasers and Electro-Optics Society (LEOS '08)*, pp. 20–21, Acapulco, Mexico, November 2008.